

## **Virtual and Physical Prototyping**



ISSN: 1745-2759 (Print) 1745-2767 (Online) Journal homepage: www.tandfonline.com/journals/nvpp20

# Autonomous printing process optimisation and in-situ anomaly detection in fused deposition modelling using an integrated data-driven approach

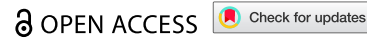
Haining Zhang, Yangwen Yu, Xingchen Liu, Nannan Liang, Yongrae Kim, Dongwoon Shin, Seung Ki Moon & Joon Phil Choi

**To cite this article:** Haining Zhang , Yangwen Yu , Xingchen Liu , Nannan Liang , Yongrae Kim , Dongwoon Shin , Seung Ki Moon & Joon Phil Choi (2025) Autonomous printing process optimisation and in-situ anomaly detection in fused deposition modelling using an integrated data-driven approach, Virtual and Physical Prototyping, 20:1, e2545523, DOI: 10.1080/17452759.2025.2545523

To link to this article: <a href="https://doi.org/10.1080/17452759.2025.2545523">https://doi.org/10.1080/17452759.2025.2545523</a>

9	© 2025 The Author(s). Published by Informa UK Limited, trading as Taylor & Francis Group
	Published online: 21 Aug 2025.
Ø.	Submit your article to this journal $oldsymbol{\mathcal{Z}}$
hh	Article views: 710
a`	View related articles 🗹
CrossMark	View Crossmark data 🗹







## Autonomous printing process optimisation and in-situ anomaly detection in fused deposition modelling using an integrated data-driven approach

Haining Zhang<sup>a</sup>, Yangwen Yu<sup>b</sup>, Xingchen Liu<sup>c</sup>, Nannan Liang<sup>a</sup>, Yongrae Kim<sup>d</sup>, Dongwoon Shin<sup>d</sup>, Seung Ki Moon<sup>e</sup> and Joon Phil Choi<sup>d</sup>

<sup>a</sup>School of Information Engineering, Suzhou University, Suzhou, People's Republic of China; <sup>b</sup>Department of Electrical and Electronic Engineering, The University of Hong Kong, Pokfulam, People's Republic of China; <sup>c</sup>Department of Industrial and Systems Engineering, Hong Kong Polytechnic University, Hong Kong, People's Republic of China; <sup>d</sup>Department of 3D Printing, Korea Institute of Machinery & Materials, Daejeon, Republic of Korea; eSchool of Mechanical and Aerospace Engineering, Nanyang Technological University, Singapore, Singapore

#### **ABSTRACT**

Fused Deposition Modelling (FDM) is the predominant material extrusion technique in polymer additive manufacturing (AM). While it offers compatibility with engineering-grade composites and enables the fabrication of polymer-composite components with intricate architectures unattainable through traditional techniques, the persistent dependence on empirical process tuning often leads to structural defects - critical limitations that hinder FDM's transition to advanced industrial applications. This paper proposes a data-driven approach that integrates advanced Artificial Intelligence (AI) with real-time computer vision to optimise FDM process parameters and enable in-process anomaly detection. In the developed approach, a stepwise machine learning strategy systematically models the printed line quality, ensuring pre-print process optimisation. A You Only Look Once (YOLO) object detection model is then deployed for in-situ monitoring, analysing the printed line morphology to assess melt flow stability and detect geometric deviations during printing. Validation experiments are conducted to assess the effectiveness of the developed YOLO model. Overall, the integrated framework demonstrates its superiority over empirical methods and analytical models in both pre-process optimisation and real-time quality assurance. Furthermore, the integrated machine vision and pattern recognition system exhibits adaptability to diverse material deposition systems, providing a unified approach to intelligent process optimisation across AM domains.

#### ARTICLE HISTORY

Received 3 June 2025 Accepted 4 August 2025

#### 1. Introduction

Additive manufacturing (AM) - encompassing technologies that construct three-dimensional (3D) objects through successive material layering - enables the customised production of polymers, ceramics, and metals, surpassing conventional manufacturing in terms of design freedom and rapid prototyping capabilities [1,2]. As a transformative facet of advanced manufacturing, AM systems exhibit exceptional material efficiency while addressing specialised application requirements through geometrically complex structures [3,4]. Among these technologies, fused deposition modelling (FDM) dominates industrial adoption due to its operational maturity. This extrusion-based process allows the fabrication of polymeric/composite components with intricate architectures that are unattainable through traditional techniques, while hybrid variants enable the production of metallic parts through post-process sintering [5,6]. As the most established AM modality, FDM combines technical versatility with sustainable innovation across the aerospace [7,8], biomedical [9,10], and automotive sectors [11,12], leveraging diverse thermoplastics and reproducible workflows to minimise material waste and energy consumption in advanced manufacturing.

FDM is distinguished among AM technologies such as stereolithography (SLA) [13,14] and selective laser sintering (SLS) [15,16] through its compatibility with lowmelting-point materials, its minimal chemical byproduct generation, and its simplified postprocessing enabled by water-soluble support structures. However, the industrial scalability of this method depends critically on precise parameter optimisation - notably the nozzle temperature, print speed, and material flow rate - as

even minor deviations in the printed line quality can induce defects that compromise part functionality [17-19]. For instance, line discontinuities caused by nozzle clogs or temperature instability can weaken interlayer adhesion, leading to delamination in structural components [20,21]. Under-extrusion, resulting from improper flow rates or layer heights, creates micro-voids and porosity in the printed lines, reducing the tensile strength and fatigue resistance [22,23]. Meanwhile, rapid cooling or mechanical vibrations can exacerbate line edge roughness, undermining the dimensional tolerances required for precision assemblies such as seals or bearings [24]. Additionally, uneven extrusion pressure or bed misalignment can cause irregular line spreading, distorting fine geometries such as microfluidic channels or threaded interfaces [25,26]. Typically, these line defects collectively degrade the surface finish, geometric accuracy, and mechanical integrity, posing barriers to applications that require high reliability under load or tight tolerances. Consequently, systematic analyses of the FDM line morphology and optimisation of related process parameters are crucial to balancing the deposition efficiency with defect reduction, ensuring that functional parts meet industrial standards with regard to strength, precision, and surface finish.

Studies show that process parameters such as the nozzle temperature, flow rate, and print speed significantly affect the FDM printing quality [27,28]. This arises from the intricate interplay between process parameters, which induces material flow dynamics that govern the precise extrusion of molten thermoplastic filaments and the stabilisation of the deposited line geometry [29,30]. Thus, research focused on optimising the extrusion uniformity and printing quality has become a central focus in FDM studies. For example, several empirical techniques that optimise the extrusion multiplier and nozzle temperature at a given print speed have been introduced, ensuring stable melt flow behaviour prior to line deposition [31,32]. However, the resulting solutions may remain suboptimal owing to the limited exploration of the design space. Similarly, finite element analysis (FEA) models have been developed to analyse the effects of the nozzle temperature, print speed, and flow rate on the melt flow dynamics in FDM, with the aim of identifying thermal parameters that are effective in ensuring a stable melt flow during extrusion [33-36]. However, developing a reliable and performance-efficient FEA model for FDM processes particularly those involving rapid thermal gradients and material solidification – poses considerable difficulty.

In contrast to FEA models, data-driven modelling offers superior efficiency and reduced dependence on prior knowledge [37,38]. However, its application in FDM optimisation has been limited by constrained objective functions, sparse datasets, and manual workflows. Nevertheless, recent advancements in integrating physicsinformed machine learning with image sensor analytics are driving the development of more robust optimisation frameworks. These developments bridge the gap between data-driven agility and physics-based rigour. allowing for efficient methods that leverage diverse visual data while respecting underlying material behaviour. For instance, Uhrich et al. [39] and Kapusuzoglu et al. [40] explored physics-informed machine learning approaches that integrate physics-based knowledge into data-driven models to predict the printing quality of FDM parts, ensuring a consistent physical relationship between process parameters and mechanical properties. On the other hand, Li et al. [41] integrated thermal, vibrational, and imaging data for printing quality optimisation; Narayanan et al. [42] used PCA with a support vector machine to classify defective polymer parts; Özen et al. [43] applied K-means clustering to link process parameters with FDM microstructure and properties. Collectively, these studies highlight the effectiveness of datadriven methods in improving the AM processes. However, the inherent susceptibilities like thermal-gradient-induced warping, material cooling shrinkage, and nozzle extrusion inconsistencies can destabilise printing quality [44-47], leading to defects and dimensional inaccuracies that reduce the functional reliability of the final products.

Recent advancements in deep learning have significantly enhanced in-situ monitoring and defect detection in FDM, owing to their ability to extract complex patterns from high-dimensional data, such as layer-wise images, thermal profiles, and acoustic signals, with minimal human intervention. For instance, convolutional neural networks (CNNs) have demonstrated remarkable success in detecting extrusion irregularities (e.g. spaghetti defects) and geometric distortions (e.g. warping or layer misalignment) by leveraging transfer learning to overcome limited training datasets [48]. Similarly, texture-based algorithms [49] and hybrid deep learning models [50,51] have enabled real-time defect diagnosis by correlating process anomalies with multisensor data. While deep learning has advanced in-situ monitoring for FDM, achieving fully autonomous, adaptive quality control remains challenging [52]. Current approaches include single-modality CNNs for visual defect detection, multi-sensor fusion models integrating thermal and acoustic data, and hybrid CNN-RNN architectures for capturing temporal variations [53,54]. Despite high detection accuracy, these systems face key limitations: limited interpretability of defect causes,

insufficient processing speed for real-time correction, and lack of integration across monitoring, diagnosis, and actuation. Therefore, integrating a comprehensive defect analysis with in-situ monitoring will enable systematic diagnosis, which is critical for improving process stability and consistency in FDM.

In this research, a data-driven framework is proposed that integrates advanced AI techniques with real-time computer vision to optimise FDM printing process and enable in-process anomaly detection simultaneously. In the developed approach, a stepwise machine learning strategy that systematically models and analyses the printed line morphology is employed, ensuring systematic process optimisation prior to printing. Subsequently, a You Only Look Once (YOLO) object detection model is deployed for in-situ monitoring. This model utilises printed line morphology to assess FDM printing status and detect anomalies during the process. Experiments further confirm the effectiveness of the proposed approach with regard to real-time process monitoring, demonstrating its potential to advance line optimisation and defect detection during FDM printing. This end-to-end pipeline enables both preemptive process calibration and corrective control within a single intelligent system. To the best of our knowledge, the present study provides a novel and transformative integration of complementary AI metrologies into a real-time, adaptive control paradigm for extrusion-based

manufacturing, establishing a new benchmark for innovation in the field.

The remaining of this paper proceeds as follows. Section 2 introduces the proposed data-driven framework for FDM process modelling and in-situ defect detection. Section 3 validates the proposed approach through experimental analysis and a real-time monitoring performance assessment. Section 4 summarises the research and suggests further directions.

#### 2. Proposed data-driven approach in FDM

#### 2.1. Overview of the proposed approach in FDM

Figure 1 outlines the proposed data-driven framework for FDM process enhancement. In Figure 1(a), dual imaging systems are integrated into the printer: a coaxial camera enables autonomous printing process optimisation prior to printing, while a process camera supports in-situ anomaly detection during printing. Figure 1(b) elaborates on the coaxial system's iterative workflow, where a stepwise machine learning approach refines the printing quality through adaptive process parameter optimisation. Parallel to this, Figure 1(c) highlights the embedded YOLO architecture of the process camera, which performs in-situ defect detection during the extrusion process. Finally, Figure 1(d1-d6) demonstrates the real-time anomaly detection capability of the system, which stabilises the printing process and

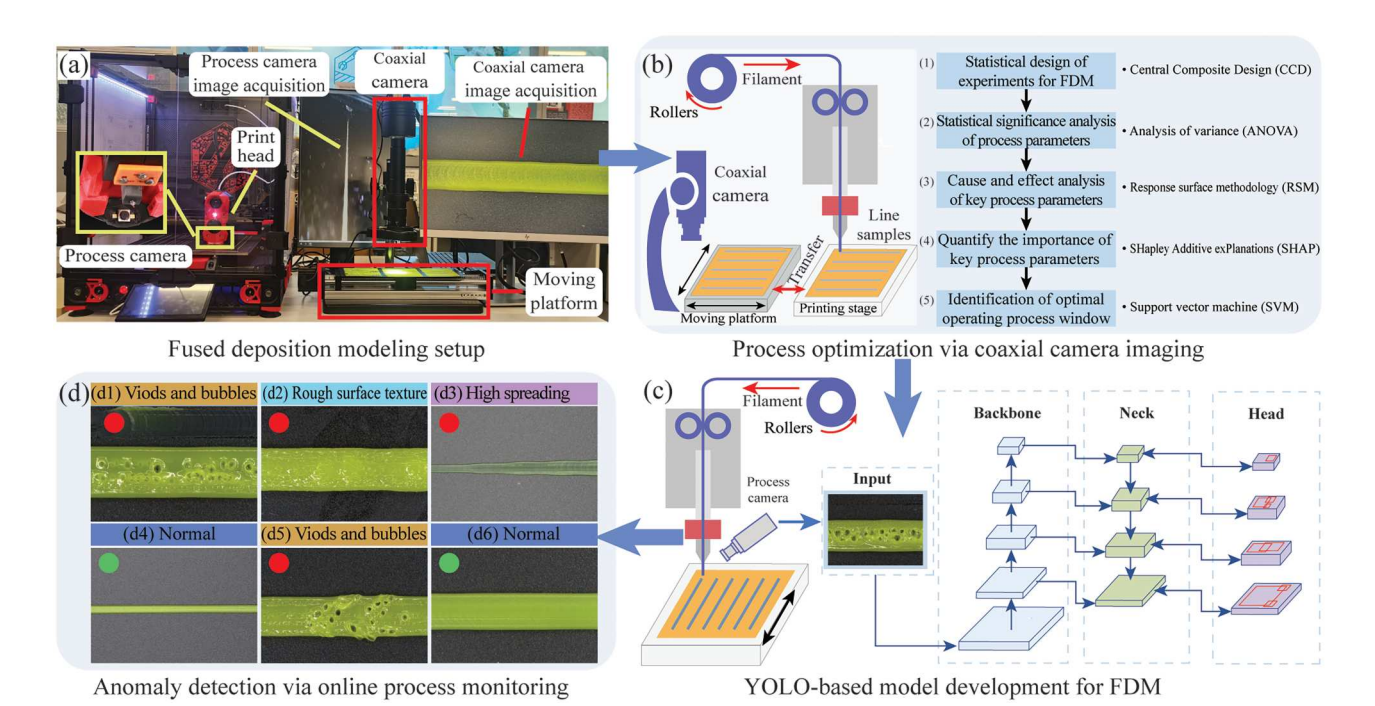


Figure 1. Integrated data-driven framework for process parameter optimisation and anomaly detection in FDM: (a) Dual-camera FDM monitoring system setup, (b) multi-stage process parameter optimisation via coaxial imaging prior to printing, (c) YOLO-based defect detection model development, and (d) YOLO-based in-situ anomaly detection with process camera feedback.

maintains consistent product quality throughout production.

# 2.2. Stepwise machine learning techniques for optimisation of the FDM process

Figure 2(a) presents a schematic illustration of a coaxial camera system integrated into an FDM 3D printer, aligned coaxially with the printhead and oriented

perpendicularly to the print bed. In this research, an 8 MP CCD colour camera is employed for image capturing, offering a resolution of  $3840 \times 2160$  pixels. Following the printing process, the printed line samples are promptly moved to the platform beneath the coaxial camera, where real-time digital images are captured, as shown in Figures 2(b–h) to support rapid process optimisation.

Specifically, the FDM optimisation process consists of five sequential stages: (1) A Central Composite Design

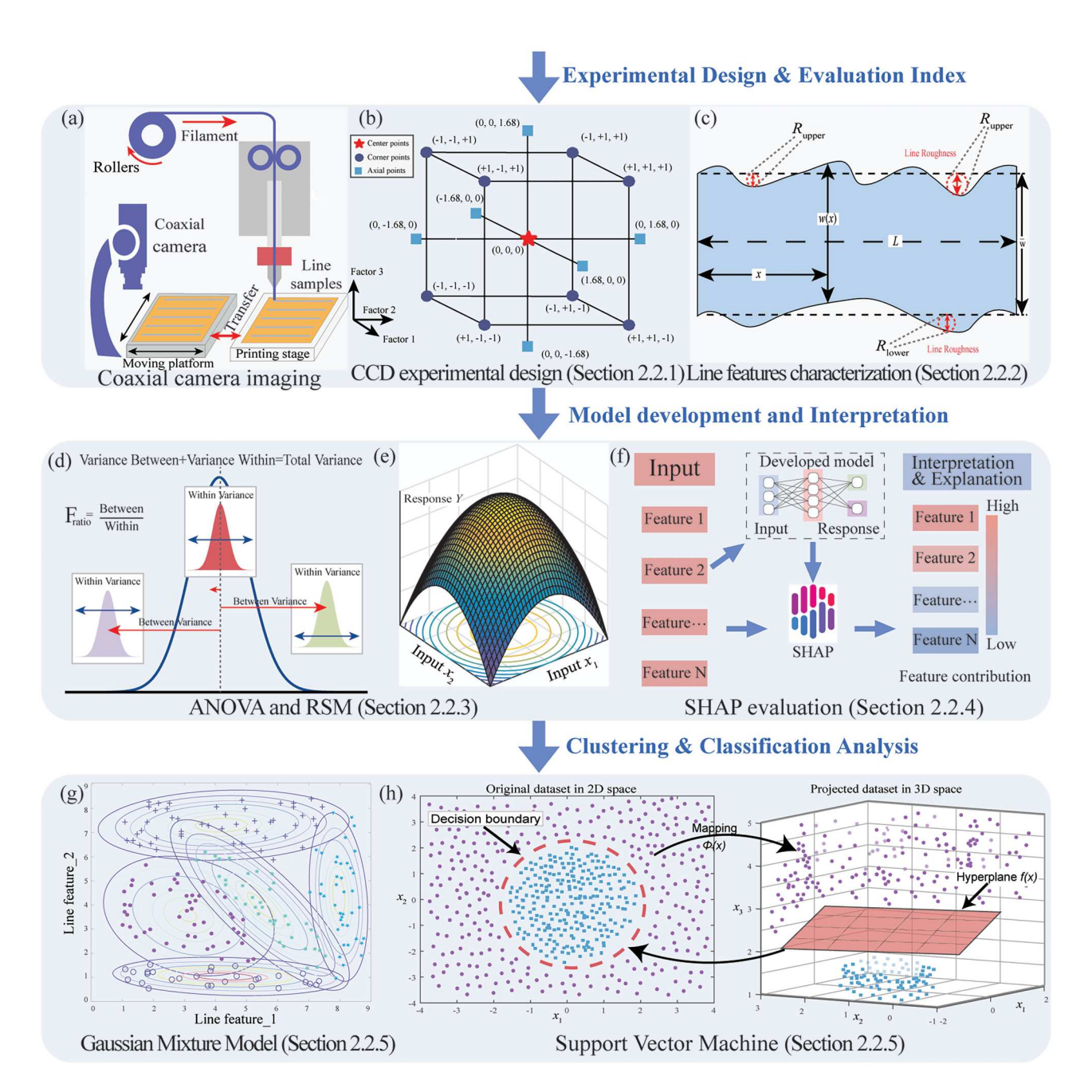


**Figure 2.** Autonomous process optimisation via a stepwise machine learning method: (a) Coaxial imaging system for in-situ line morphology monitoring, (b) CCD of FDM process parameters, (c) Geometric characterisation of deposited lines, (d) ANOVA for parameter significance evaluation, (e) RSM modelling of parameter-response relationships, (f) SHAP analysis for feature importance quantification, (g) GMM-based clustering of line morphology distributions, and (h) SVM-based classification for optimal process window identification.

Table 1. Five-stage autonomous optimisation workflow for FDM process parameters: From experimental design to operational window identification via CCD, ANOVA, RSM, SHAP, GMM and SVM methodologies.

Step	Inputs	Approaches	Responses
1	Design space: { Nozzle temperature, Flow rate multiplier, Layer thickness, Print speed, Pressure advance}	CCD experimental design	<ul> <li>Designed experimental points: (Nozzle temperature, Flow rate multiplier, Layer thickness, Print speed, Pressure advance)</li> </ul>
2	Experimental points: (Nozzle temperature, Flow rate multiplier, Layer thickness, Print speed, Pressure advance)	Coaxial camera imaging and characterisation of printed line features	<ul> <li>Mean line width (w̄)</li> <li>Line discontinuity (L<sub>disc</sub>)</li> <li>Mean line edge roughness (R<sub>m</sub>)</li> <li>Mean line density (L̄<sub>ρ</sub>)</li> </ul>
3	<ul> <li>(\(\bar{w}\), \(R_m\))</li> <li>(Nozzle temperature, Flow rate multiplier, Layer thickness, Print speed, Pressure advance)</li> </ul>	ANOVA, RSM and SHAP	<ul><li>Significance analysis</li><li>Correlation analysis</li><li>Feature importance analysis</li></ul>
4	$(\overline{L_{\rho}}, R_m, L_{disc})$	GMM	Distribution of printed line morphology
5	<ul> <li>Labeled lines (abnormal/normal)</li> <li>(Nozzle temperature, Flow rate multiplier, Print speed)</li> </ul>	SVM	Identified optimal operational window

(CCD) approach efficiently explores the design space, maximising coverage with minimal experimental data. (2) An inline coaxial camera system, paired with automated image analysis, characterises printed line samples generated under the CCD framework. (3) Analysis of variance (ANOVA) identifies significant process parameters, while response surface methodology (RSM) models the inputoutput relationship to guide optimisation. (4) SHAP (Shapley Additive Explanations) quantifies the contributions of significant variables, selecting those critical for further optimisation. (5) A Gaussian Mixture Model (GMM) analyses the distribution of printed line patterns, and a Support Vector Machine (SVM) distinguishes normal from abnormal lines, defining an optimal operating window to ensure consistent FDM printing quality. Table 1 presents a comprehensive workflow corresponding to Figure 2, outlining the key steps, inputs, approaches, and responses for each stage of the process.

#### 2.2.1. CCD statistical experiments

The nonlinearity in the FDM 3D printing process, caused by complex thermal gradients and material deposition dynamics, requires an experimental design that can capture these nonlinearities [55,56]. In this research, CCD is implemented to systematically analyse nonlinear interactions and curvature effects. As shown in Figure 2(b), CCD combines factorial points to examine linear and interaction effects, axial points to measure quadratic terms, and centre points to assess process variability through controlled iterative testing.

#### 2.2.2. Printing quality analysis of FDM

Effective process optimisation in FDM requires a quantitative assessment of the extrudate morphology. This study establishes four key quality metrics through an image analysis [54,57]. Specifically, as shown in Figure 2(c), the mean line width  $\bar{w}$  is computed via the column-wise spatial averaging of pixel intensity data in a discretized form

$$\bar{w} = \frac{1}{N} \sum_{i=1}^{N} w_i \tag{1}$$

Then, the greyscale intensities of pixels bounded by the identified edges of printed lines are averaged to compute the mean line density  $\overline{L_o}$ 

$$\overline{L_{\rho}} = \frac{1}{N} \sum_{i=1}^{N} I_i - I_b \tag{2}$$

Subsequently, based on the obtained reference lines (mean lines), the average line edge roughness  $R_m$  and line discontinuity  $L_{disc}$  are defined below,

$$R_{m} = \sqrt{\frac{1}{2N} \sum_{i=1}^{N} (R_{upper,i}^{2} + R_{lower,i}^{2})}$$
 (3)

$$L_{disc} = \frac{F_u + F_l}{2N} \tag{4}$$

In addition, the overall printing quality  $L_q$  is calculated by combining the key aspects of the printed lines with assigned weights.

$$L_a = W_o \times \overline{L_o} + W_r \times R_m + W_d \times L_{disc} \tag{5}$$

where  $w_i$  represents the quantised line width in the *i*th column, with N being the total number of columns.  $I_i$  is the average intensity per column, and  $I_b$  is the mean background intensity to reduce illumination effects.  $R_i$  captures deviations from the mean line edge, while  $F_u$  and  $F_l$  denote



failures in detecting the upper and lower edges.  $W_{\rho}$ ,  $W_{r}$  and  $w_{sp}$  are the weighting coefficients for density, edge roughness, and discontinuities in the printed lines, respectively.

#### 2.2.3. ANOVA analysis and RSM modelling

ANOVA evaluates the statistical significance of FDM process parameters using CCD-designed experiments by quantifying individual parameter effects and detecting interactions. It decomposes variance into systematic (factor-driven) and random (error) components, using Ftests and p-values (p < 0.05) to identify meaningful variables amid experimental noise [55]. This method aids in identifying dominant factors and interactions for optimised FDM processes. As shown in Figure 2(d-e), RSM builds on ANOVA-identified factors to create empirical models linking FDM inputs to key outputs. By performing quadratic regression on CCD data, RSM quantifies nonlinear relationships and parameter interactions while filtering noise. It resolves multi-parameter trade-offs that one-variable methods cannot, and the resulting second-order polynomial equations predict responses across the design space, guiding FDM process optimisation.

#### 2.2.4. Interpretability and quantification of process parameter contributions

Building on statistically significant variables, their contributions can be systematically evaluated to guide adjustments in subsequent experiments or operations. As shown in Figure 2(f), SHAP is effective for this, as it uses Shapley values to quantify feature contributions by assessing their impact across all possible feature combinations in model predictions [58,59]. SHAP offers both global interpretability, showing the overall importance of variables, and local interpretability, highlighting individual feature impacts on specific predictions. This dual approach ensures transparency and consistency, while its rigorous method provides precise quantification of effects.

### 2.2.5. Process-parameter impact analysis and operational optimisation

The intricate dynamics of thermoplastic extrusion, thermal gradients, and layer adhesion in FDM significantly affect extruded line morphology and dimensional accuracy. This study uses GMM to quantify the impact of critical parameters on the statistical distribution of printed line patterns. As shown in Figure 2(g), GMM efficiently handles multimodal data and variability, enabling precise identification of parameter-driven effects on extrusion behaviour, outperforming traditional clustering methods [60,61]. By using extrudate characteristics ( $\overline{L_{\rho}}$ ,  $R_m$ ,  $L_{disc}$ ) as inputs, GMM categorises morphological deviations caused

parameters, establishing relationships that guide adjustments to avoid defects. Since FDM printing quality is highly sensitive to parameter combinations, suboptimal settings can lead to geometric irregularities, compromising mechanical performance and dimensional precision. To address this, the study employs an SVM to identify an optimised parameter window. As illustrated in Figure 2(h), SVM constructs a hyperplane in high-dimensional feature space to distinguish stable parameter configurations, leveraging its resistance to overfitting and ability to model nonlinear relationships [62,63]. This approach systematically defines stable processing windows, minimising defects and ensuring consistent extrudate quality.

### 2.3. YOLO model for in-situ anomaly detection in printed line morphologies

Figure 3 illustrates the in-situ monitoring method for the FDM 3D printing process using YOLOv5. As shown in Figure 3(a), a process camera is positioned adjacent to the printhead to capture the real-time line deposition quality under the nozzle. In this study, a 1080P CCD colour camera (1920 × 1080 pixels) is employed for insitu process monitoring. In Figure 3(b), images of deposited lines are annotated to create a training dataset for YOLOv5, which is developed to detect and localise printing defects. Figure 3(c) demonstrates how real-time defect detection results from sequentially captured images are analysed to assess the printing status. If anomalies are identified (Figure 3(d)), process parameters are adjusted using correlations from the developed RSM models to mitigate defects and improve the printing quality.

#### 2.3.1. Line morphology classifier development using YOLO architectures

CNNs form the foundation of deep learning frameworks for computer vision tasks, with YOLO standing out as a preferred architecture for both object detection and defect recognition [64]. Unlike traditional classificationoriented CNNs, YOLO integrates backbone, neck, and head modules to localise defects (via bounding box regression) and classify defect types simultaneously, which is critical for halting print failures before they propagate [65].

For FDM process monitoring, YOLOv5 offers particular advantages due to its optimised balance of inference speed, detection accuracy, and compatibility with embedded systems. Its architecture leverages Cross Stage Partial Darknet 53 (CSPDarknet53) as the backbone for feature extraction, the Path Aggregation Network (PANet) for multi-scale feature fusion, and

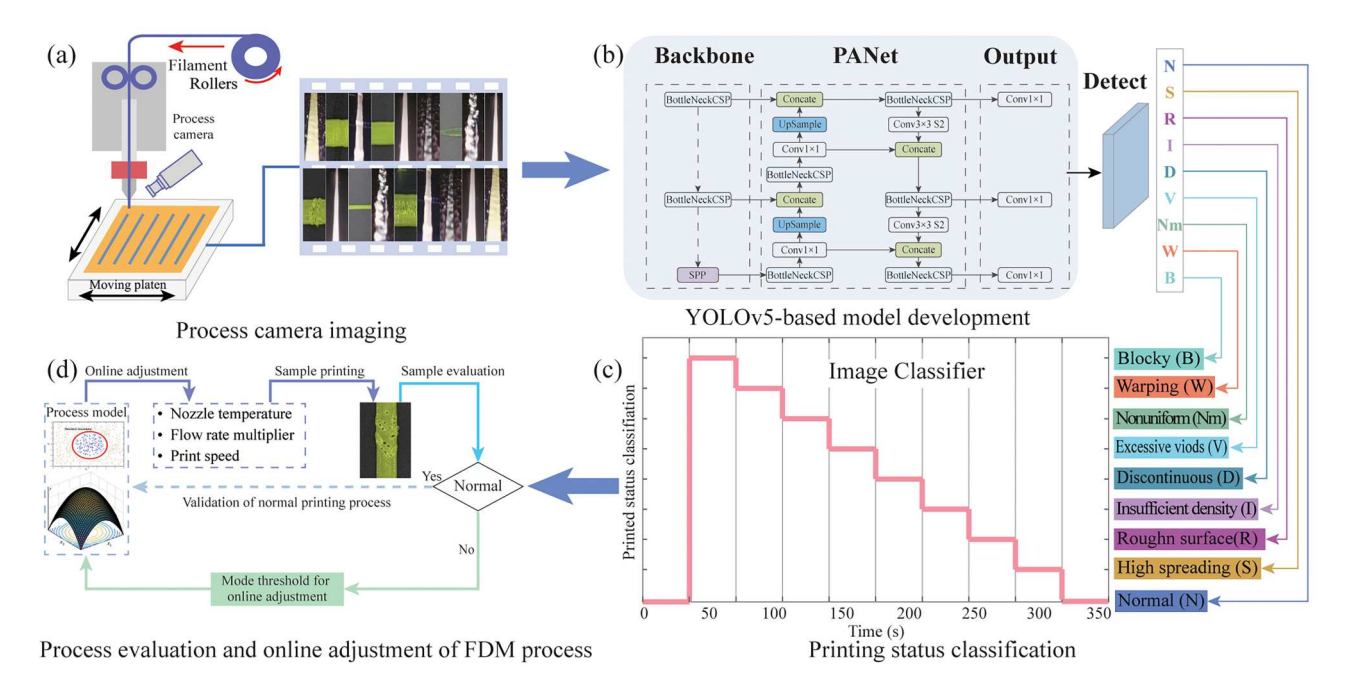


Figure 3. YOLOv5-enabled FDM process monitoring system. (a) In-situ deposition monitoring setup, (b) YOLOv5 defect detection pipeline development (Backbone→PANet→Output), (c) time-dependent printing status assessment using the developed YOLOv5 model, and (d) dynamic process parameter adjustment via RSM-based optimisation.

anchor-based detection heads for bounding box predictions [66,67]. Noteworthy innovations include mosaic data augmentation to enhance model generalisation, adaptive anchor box tuning tailored to FDM-specific defect sizes, and auto-learning bounding box priors to reduce the need for manual calibration. In this study, the total loss function (Ltotal) in YOLOv5 integrates three essential components for defect detection. Specifically, the bounding box loss ( $L_{box}$ ) quantifies the difference between the predicted and ground truth bounding box coordinates, the object loss  $(L_{object})$ assesses the confidence that an object is present within a predicted bounding box, and the classification loss ( $L_{class}$ ) classifies defect categories while addressing class imbalance issue [68].

$$L_{box} = 1 - IoU + \frac{\rho^2(b_{pred}, b_{gt})}{c^2} + \alpha v$$
 (6)

$$L_{object} = -\sum_{i=0}^{S^2} [y_i \log(p_i) + (1 - y_i) \log(1 - p_i)]$$
 (7)

$$L_{class} = -\sum_{c=1}^{C} [y_c \log (p_c) + (1 - y_c) \log (1 - p_c)]$$
 (8)

$$L_{total} = \lambda_{box} L_{box} + \lambda_{object} L_{object} + \lambda_{class} L_{class}$$
 (9)

Here  $L_{box}$  integrates the IoU (area overlap ratio), the centre distance (p) between the centres of the predicted  $(b_{pred})$  and ground truth  $(b_{at})$  boxes, the enclosing box diagonal (c), and the aspect ratio consistency (v) weighted by  $\alpha$ ;  $L_{object}$  computes the binary cross-entropy across  $S^2$ grid cells between the ground truth presence  $(y_i)$  and predicted probability  $(p_i)$ ;  $L_{class}$  uses the cross-entropy over C classes comparing true indicators  $(y_c)$  and predicted probabilities ( $p_c$ ). Moreover,  $\lambda_{box}$ ,  $\lambda_{object}$ , and  $\lambda_{class}$  are hyperparameters tuned to achieve a balance between high detection accuracy and fast inference for FDM real-time object detection tasks.

#### 2.3.2. Anomaly detection and status evaluation

This study focuses on real-time process monitoring for FDM by classifying printed line morphology into nine defect categories: 'Discontinuities' (D), 'Insufficient density' (I), 'High spreading' (S), 'Rough surface texture' (R), 'High warping' (W), 'Nonuniform distribution' (Nm), 'Blocky deposition pattern' (B), 'Excessive voids and bubbles' (V), and 'Normal line' (N). These categories identify common extrusion issues caused by factors like thermal gradients, material flow inconsistencies, and mechanical misalignments. A mode-detection algorithm tracks prediction frequencies across consecutive printed lines. When an abnormal category exceeds a statistically determined threshold, indicating systemic defects, the system triggers compensatory adjustments based on a RSM model that maps key parameterresponse relationships. Calibration defines tuning increments while balancing the correction speed and stability to prevent overcompensation oscillations. If no

Table 2. Experimental setup of the FDM process.

	Adjustable process variables				Work	Environment	
Nozzle temperature	Flow rate multiplier	Pressure advance	Layer thickness	Print speed	Bed temperature	Tip diameter	Material
100°C	50-200%	0-2 s	0.1-0.3 mm	60-900 mm/min	100°C	0.4 mm	PLA

dominant defect mode is detected or predictions remain 'Normal,' the parameters remain unchanged to maintain process consistency. This approach allows efficient defect mitigation in real-time, avoiding the need for post-hoc inspection, and enhances dimensional accuracy in complex geometries prone to process-induced distortions.

#### 3. Experimental results and discussion

#### 3.1. Experimental setup

This study utilised an open-source Voron FDM 3D printer for data acquisition, chosen for its cost-effectiveness, integrated bootloader, and built-in Z-probe. A Raspberry Pi 4 Model B functioned as a networked serial gateway, enabling real-time bidirectional communication via the USB-CDC protocol. Building on this hardware foundation, a CCD design was implemented with coded factor levels spanning centre (0), factorial (±1), and axial (±1.68) points, as mathematically formalised in Appendix Table A1. Specifically, the nozzle temperature, flow rate multiplier, layer thickness, pressure advance, and print speed are considered as the independent input factors, with the printed line edge roughness and line width investigated as target responses.

During printing, each experimental point, which was varied according to the CCD design and replicated three times, generated a single-pass line sample with distinct morphometric attributes deposited on a substrate; the printed line morphology was immediately measured using an Olympus microscope, and the profiles were analysed via an image processing algorithm. The detailed FDM experimental setup is summarised in Table 2.

Meanwhile, to build a comprehensive data-set with which to develop a YOLO classifier, a CCD process camera was employed to obtain images of various printing states by altering adjustable process variables within a defined design space. These states were grouped into nine categories: 'Discontinuities,' 'Insufficient density,' 'Excessive spreading,' 'Rough surface texture,' 'High warping,' 'Nonuniform distribution,' 'Blocky deposition pattern,' 'Excessive voids and bubbles,' and 'Normal line.' To increase the robustness of the developed model and diversify the dataset, additional augmentations such as lighting variations, image flipping, resizing, and rotation were applied, along with samples from different materials and colours. In total, 9,396 printed line images were generated, with 80% designated for training and 20% for validation. Figure A1 shows the experimental points in the design space, which were obtained through Latin Hypercube Sampling (LHS) for further process optimisation [69,70].

#### 3.2. Process optimisation of FDM

#### 3.2.1. ANOVA of CCD derived models

The CCD-derived target responses (Appendix Table A2) are analysed using quadratic regression models to quantify the relationships between the process parameters and the printed line characteristics. ANOVA confirmed the statistical significance of both the models and individual factors, validating their predictive capability for process-response interaction.

**Table 3.** The ANOVA results of CCD study.

	R1	1	R	2
Factors	F value	P value	F value	P value
Model	168.98	<0.0001	78.79	<0.0001
Α	474.43	< 0.0001	79.82	< 0.0001
В	333.74	< 0.0001	182.87	< 0.0001
D	59.41	< 0.0001		
E			213.59	< 0.0001
AB	20.74	< 0.0001	6.75	0.0106
AE			90.27	< 0.0001
BD	6.22	0.0140		
$A^2$	119.35	< 0.0001	28.85	< 0.0001
$B^2$			10.33	0.0017
$E^2$			21.13	< 0.0001
$R^2$	0.8973		0.8468	
Adj. R <sup>2</sup>	0.8920		0.8361	
Adeq. precision	40.445		33.84	

Table 3 details ANOVA results evaluating responses R1 (line width) and R2 (line edge roughness), with factors A (nozzle temperature), B (flow rate multiplier), C (pressure advance), D (layer thickness), and E (print speed), alongside interactions (e.g. AB, AC), P-values and F-values assessed model significance: low P-values denoted statistically impactful factors, while elevated F-values confirmed that the model-derived variation outweighed the inherent process variability. Non-significant interactions (AD for R1, BE for R2) were methodically eliminated to strengthen model validity. The lackof-fit test, with P-values smaller than 0.05, confirmed that residual errors were negligible relative to replicate variability, further supporting the adequacy of the model. High R<sup>2</sup> values indicated robust explanatory power, capturing the main response variability, while Adequate Precision ratios (>15) validated a sufficient signal-to-noise resolution for practical use [55]. Generally, the CCD model effectively isolated critical parameter effects and interactions, predicted the line width (R1) and edge roughness (R2) with accuracy, and identified key parameters for quality-driven process optimisation.

To evaluate the modelling accuracy, studentized residuals (expressed in standard deviation units) were analysed. Figure 4(a,b) presents normal probability plots for the target responses, where the residuals adhere closely to a straight-line distribution with little

scatter, confirming the statistical validity of the models. Figure 4(c,d) shows the residuals plotted against the experimental test order: the random dispersion of data points around the central axis - devoid of discernible patterns – verifies their independence from temporal sequencing, thereby eliminating the test order as a confounding factor in the CCD models. Figure 4(e,f) compares predicted versus actual printed line features using a reference line (y = x). The high coefficient of determination and adequate precision values indicate robust model performance, successfully capturing causal relationships between key process parameters and printed line features. Collectively, ANOVA results confirm the reliability of the developed CCD model for both further process optimisation and prediction in FDM printing, yielding mathematical expressions (in coded units) that quantify the influence of each parameter on the printed line features, as follows:

$$R1 = 1.11 + 0.2881A + 0.2416B - 0.1019D + 0.0667AB + 0.0365BD - 0.3205A^{2}$$
 (10)

$$R2 = 0.2303 + 0.0133A + 0.0201B + 0.0217E$$
$$-0.0043AB - 0.0156AE - 0.0179A^{2}$$
$$-0.0107B^{2} + 0.0153E^{2}$$
(11)

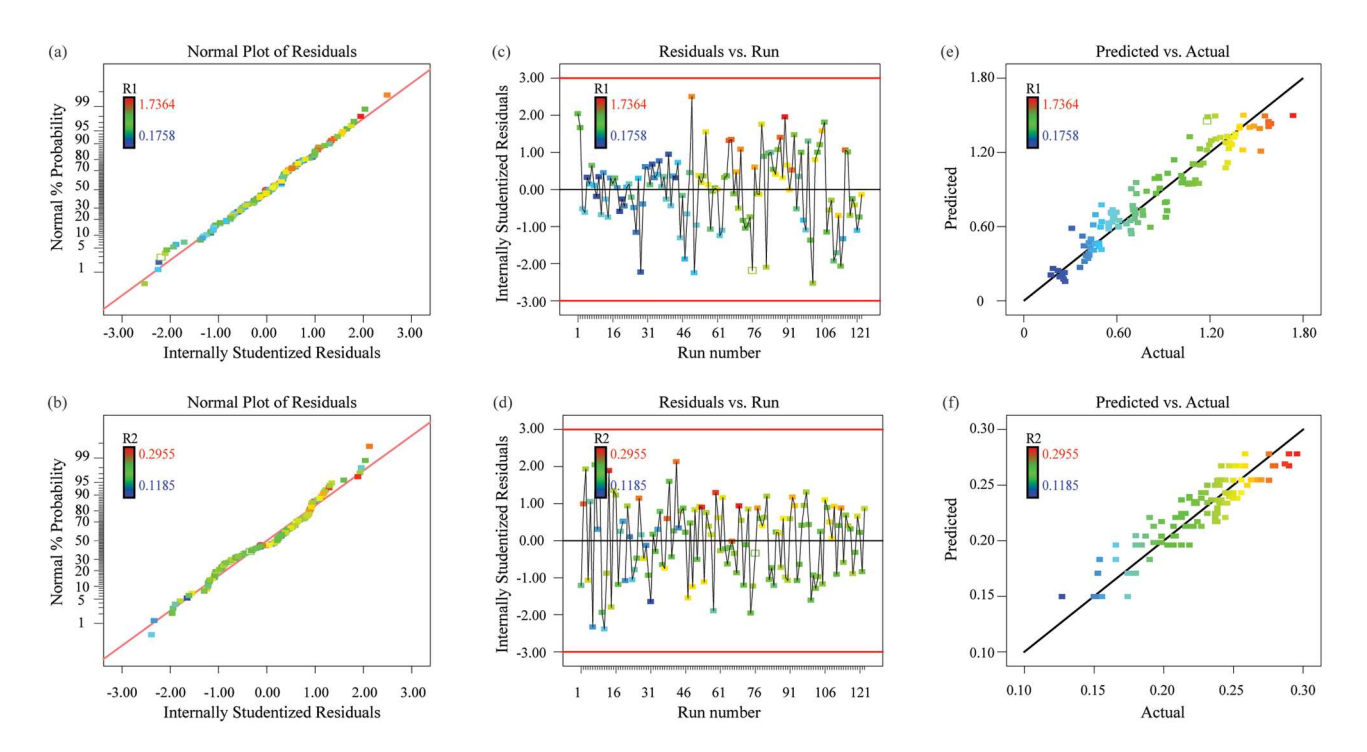


Figure 4. Residual analysis and model validation for the printed line width (PLW) and line edge roughness (LER): (a-b) Normal probability plots of residuals (PLW: a; LER: b), (c-d) Residuals vs. test orders (PLW: c; LER: d), and (e-f) Predicted vs. actual correlations (PLW: e; LER: f).

#### 3.2.2. Analysis of process parameter effects based on RSM

To enable predictive process adjustments and timely deviation compensation in FDM, establishing reliable input-output correlations between process variables and outcomes is imperative. Guided by ANOVA insights, RSM was implemented for systematic modelling of these relationships. In Figure 5, each subfigure visualises the interactive effects between two parameters on printed line feature, while non-varying parameters remain fixed at their average values.

Specifically, Figure 5(a-c) illustrates the relationships between the line width and the independent variables (nozzle temperature, flow rate multiplier, layer thickness). The plots reveal a positive linear correlation between the nozzle temperature and line width, whereas the flow rate multiplier and layer thickness show weaker linear effects. Interaction effects, such as the nozzle temperature x flow rate multiplier, induce nonlinear variations in the line width. The quadratic term for the nozzle temperature dominates the response surface curvature, manifesting as a concave shape that signifies a diminishing line width at higher nozzle temperatures. Figure 5(d-f) presents the effects of the nozzle temperature, flow rate multiplier, and print speed on the edge roughness. All three variables exhibit positive linear trends, though the nozzle temperature and flow rate act more gradually than the print speed. Interactions such as the nozzle temperature × flow rate multiplier and nozzle temperature × print speed reduce the roughness when these parameters increase

concurrently. Quadratic effects further modulate the response: the nozzle temperature<sup>2</sup> and flow rate<sup>2</sup> suppress the roughness, while the print speed<sup>2</sup> exacerbates it. The interdependent linear, interaction, and quadratic effects in the response surfaces collectively justify RSM modelling for process optimisation.

## 3.2.3. SHAP – order of importance of the key process parameters

Moreover, as shown in Figure 6, SHAP quantifies the contributions of statistically significant variables, selecting critical ones for subsequent optimisation. Specifically, Figure 6(a) reveals that the nozzle temperature, flow rate multiplier, and layer thickness are ranked by importance (highest to lowest), with the nozzle temperature having the greatest impact. SHAP values demonstrate that the nozzle temperature and flow rate positively affect the line width at high parameter values but negatively do so at low ones, while the layer thickness follows the opposite trend. This nonlinear behaviour may stem from interaction effects between parameters. In Figure 6(b), the print speed is identified as the parameter most strongly influencing the line width, followed by the flow rate multiplier and nozzle temperature. SHAP values corroborate that interactions between these parameters amplify the roughness at elevated values but suppress it at lower ones, demonstrating the nonlinear dynamics observed earlier. Given the comparable significance of the nozzle temperature, flow rate multiplier, and print speed - and the minimal influence of the layer thickness – the optimisation strategy prioritises adjustments to the first three parameters. The

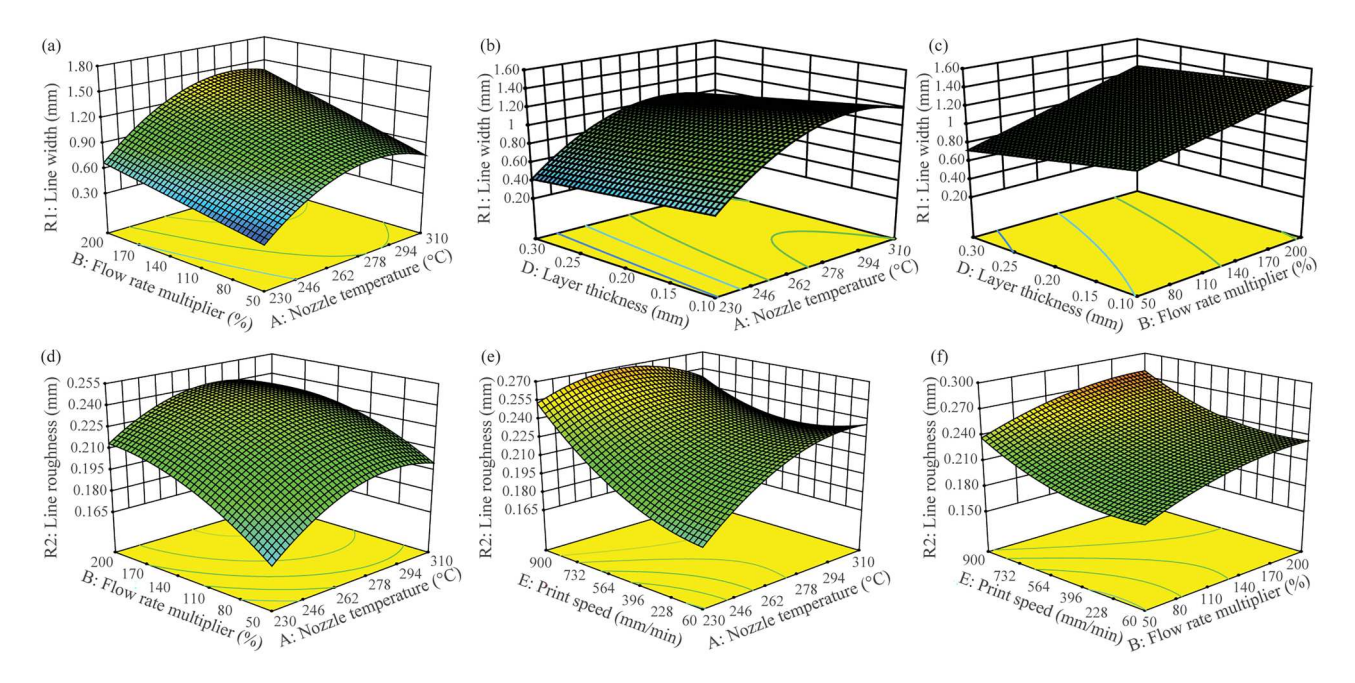
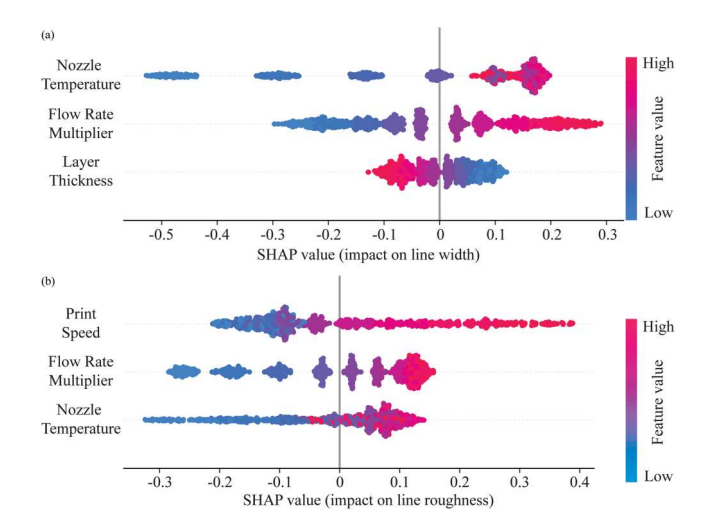


Figure 5. RSM-based analysis of process parameter effects on deposited line features: (a-c) Printed line width and (d-f) printed line edge roughness.



**Figure 6.** SHAP-based feature importance explanation of the FDM process: effects of input factors on (a) the printed line width and (b) the printed line edge roughness.

layer thickness is fixed at its median value to isolate its negligible effect.

Generally, the obtained results demonstrate strong alignment between RSM and SHAP analyses, confirming the robustness of the findings. Figure 5 reveals that nozzle temperature exerts the most significant influence on line width, followed by flow rate multiplier.

For edge roughness, print speed is the primary factor, in agreement with SHAP results presented in Figure 6. Both methods also identify key interactions, such as the nozzle temperature × flow rate multiplier in RSM and parameter-dependent nonlinearities in SHAP. The minimal impact of layer thickness in both analyses justifies its exclusion from the optimisation process.

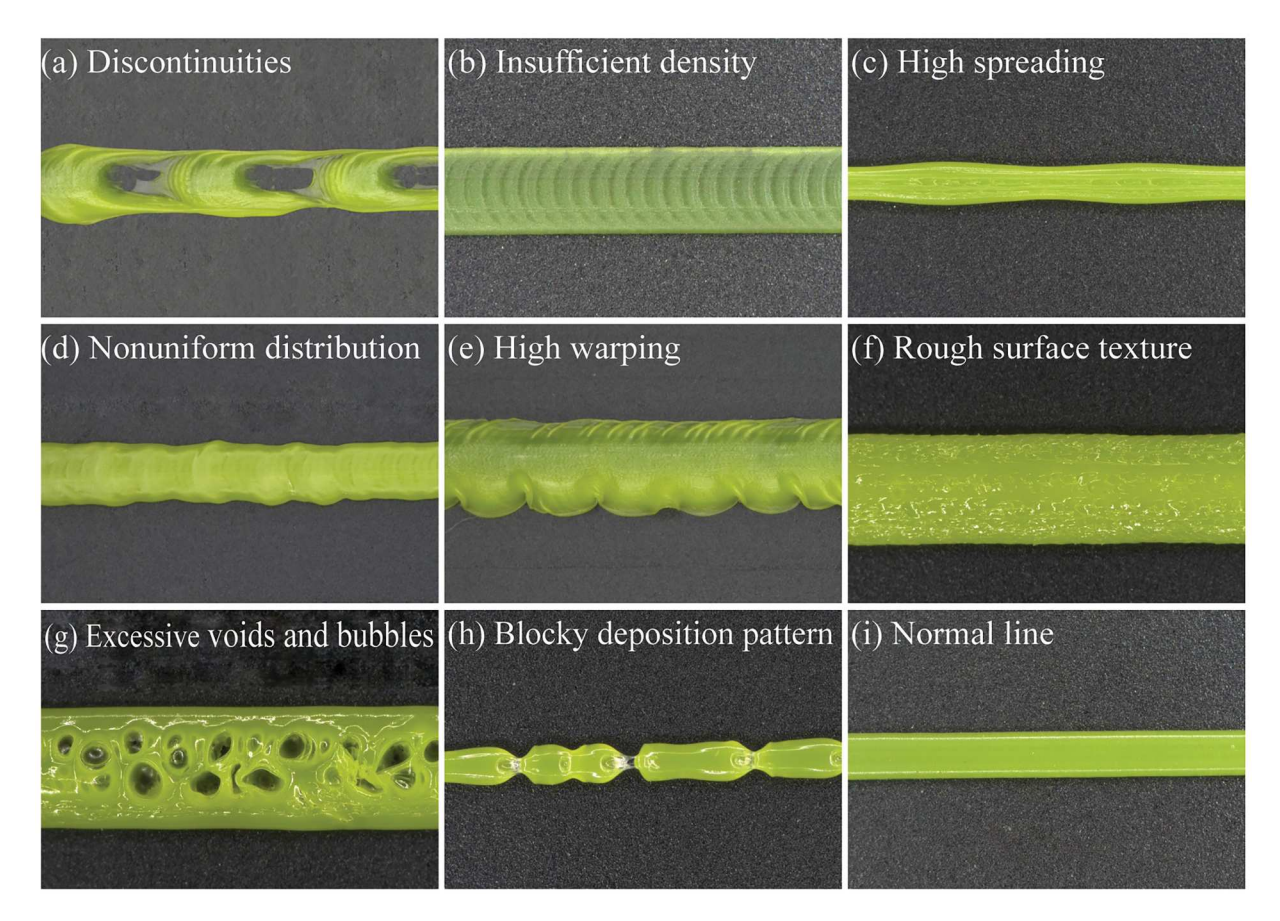
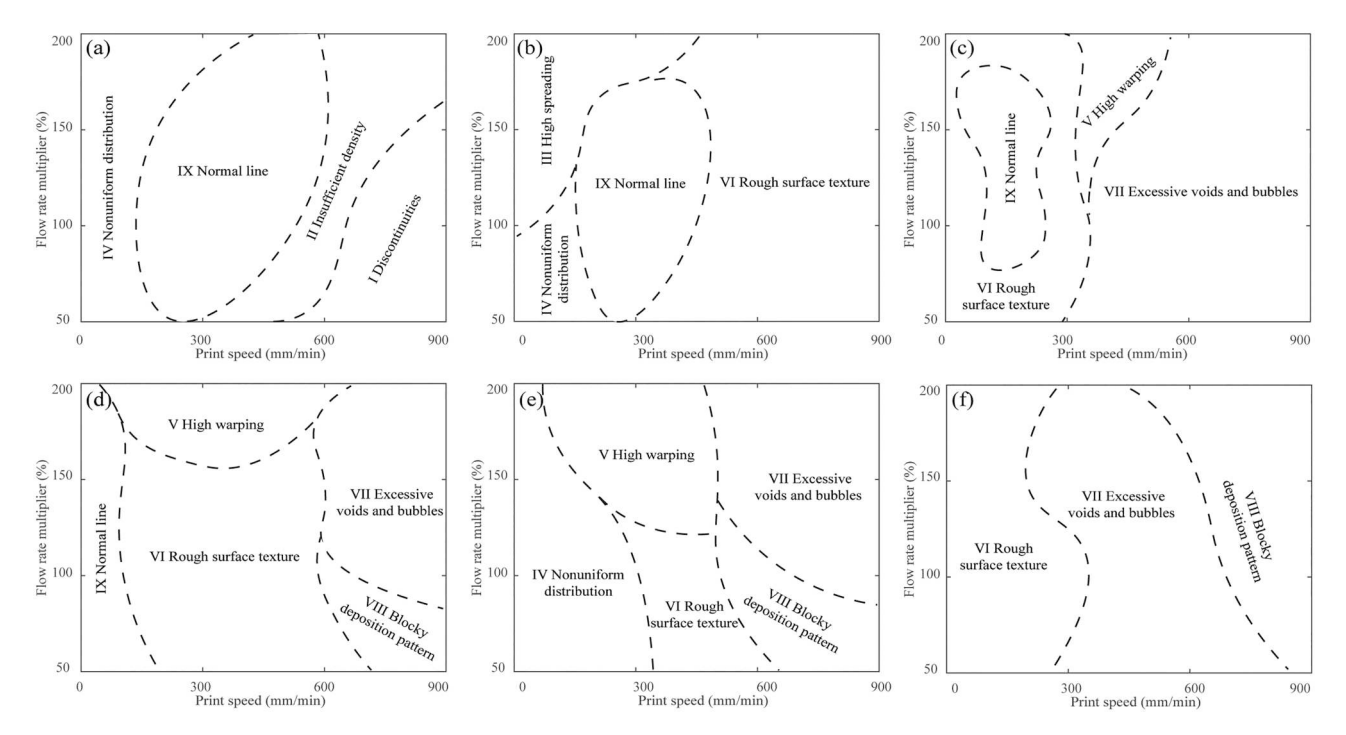


Figure 7. Instances of nine distinct printed line shapes obtained under different operational conditions.



**Figure 8.** Distribution of the printed line morphology at nozzle temperatures of (a) 230°C, (b) 250°C, (c) 270°C, (d) 290°C, (e) 310°C, and (f) 320°C.

Overall, the complementary insights from RSM and SHAP offer a solid foundation for fine-tuning parameters in FDM.

# 3.2.4. Printed line pattern analysis and process window optimisation

Images of printed line samples generated through an LHS experimental design were analysed using a Matlab® algorithm. Three key metrics of the printed line quality – the line edge roughness  $(R_m)$ , line discontinuity ( $L_{disc}$ ), and line density ( $\overline{L_{\rho}}$ ) – were adopted to analyse the distribution of printed line patterns. Based on a GMM clustering analysis, as shown in Figure 7, the printed line morphology can be classified into nine characteristic types: (a) discontinuities, (b) insufficient density, (c) high spreading, (d) non-uniform distribution, (e) high warping, (f) rough surface texture, (g) excessive voids/bubbles, (h) blocky deposition patterns, and (i) normal lines. Generally, this quantitative clustering analysis of the printed line pattern distribution facilitates the objective differentiation of various printed line patterns and aids in distinguishing normal lines from defective ones.

Specifically, Figure 8(a–f) illustrates the overall trend of the printed line morphology distribution obtained through GMM clustering, revealing significant changes with an increase in the nozzle temperature. Initially, in Figure 8(a), the printed lines display a normal line morphology within a stable distribution range, indicating minimal influence of the print speed. As the nozzle

temperature rises in Figure 8(b,c), the emergence of rough surface textures and high warping signals a decline in the printing quality due to alterations in the material flow properties. In Figure 8(d), excessive voids and bubbles become prominent alongside high warping, reflecting the detrimental impacts of elevated temperatures on material consistency. Figure 8(e) highlights the appearance of non-uniform distributions and irregular surface textures, emphasising the critical need for precise temperature management to maintain the printing quality. Finally, according to Figure 8(f), the morphology is severely compromised, with widespread defects such as voids and rough textures dominating the distribution, underscoring the challenges posed by increased temperatures during the FDM printing process. Overall, the GMM clustering approach effectively captures these trends, illustrating the complex relationship between the main process parameters and the quality of the printed lines.

To define a reliable operational range within the design space, the printing quality metric  $L_q$  was evaluated against a predetermined threshold. Printed lines in the training dataset were labelled as either normal or defective based on this threshold. An SVM model was then trained to identify the decision boundaries of the optimal operating region. The resulting 2D operational windows at nozzle temperatures of 230°C, 250°C, 279°C, and 290°C are shown in Figure 9(a). Additionally, by incorporating more samples across the 3D design space, the 3D operational window was

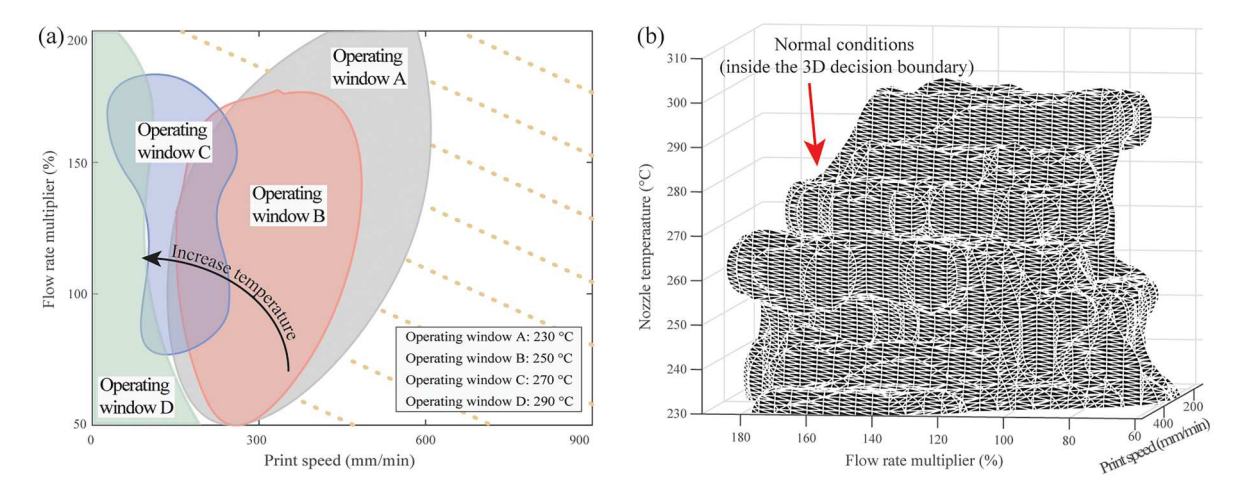


Figure 9. Process parameter optimisation of the line morphology in (a) the 2D and (b) 3D operational domains.

determined, as shown in Figure 9(b). The developed model achieved a classification accuracy rate of 93.1%, demonstrating its effectiveness in optimising the interplay among the key adjustable process variables during the fabrication process.

#### 3.2.5. Print speed effects on line defect formation

This study investigates the influence of several key process parameters on the quality of FDM prints, including nozzle temperature, flow rate multiplier, layer thickness, and pressure advance. Among these, print speed emerges as a particularly critical factor, as it directly affects the residence time of molten thermoplastic near the nozzle exit. This, in turn, influences material deposition rate, cooling behaviour, and interlayer adhesion. Specifically, a higher print speed reduces the deposition time per unit length, which may lead to inadequate bonding and extrusion instability due to insufficient heating or pressure buildup during extrusion. These issues can manifest as surface roughness, voids, or incomplete fusion between layers, ultimately compromising the overall quality of the printed object.

To quantitatively substantiate this relationship, CCD-based statistical methods, including ANOVA and RSM, are employed in this research for a comprehensive analysis. The results, as shown in Table 3 and Figure 5(d-f), identify print speed as one of the most significant parameters influencing line defects, particularly under high nozzle temperatures. Furthermore, the SHAP analysis (Figure 6(b)) quantitatively ranks print speed as the most influential variable affecting line edge roughness among all evaluated parameters, including nozzle temperature and flow rate multiplier. Additionally, the GMM clustering results reveal that defect classes, such as 'discontinuities' and 'rough textures,' are more prevalent in high-speed printing

scenarios. To further validate these findings under varied printing conditions, a series of comprehensive experiments are conducted across a broad design space – including print speeds ranging from 60 to 900 mm/min – along with variations in nozzle temperature, flow rate, and pressure advance. This extensive parameter sweep, detailed in Appendix Figure A1, further reinforces the conclusion that print speed has a critical impact on printing quality.

#### 3.3. In-situ anomaly detection of FDM

# 3.3.1. Line morphology classifier development and model comparison

In this research, YOLOv5 was implemented using the official Ultralytics repository for real-time object detection, while EfficientNet [71] and MobileNetV3 [72] were deployed using TensorFlow with ImageNet pre-trained weights as initialisation. All models were trained using a batch size of 16, the Adam optimiser, and an initial learning rate of 0.001, with a learning rate scheduler applied to ensure stable convergence. Moreover, early stopping, based on validation accuracy, was employed to prevent overtraining, while dropout layers were integrated into the EfficientNet and MobileNetV3 models to further mitigate overfitting. Input images were resized to 224 × 224 pixels and normalised using the mean and standard deviation computed from the training dataset to ensure consistent and accelerate convergence across models. In addition, the data augmentation techniques, including random rotations, translations, scaling, and colour jittering, were applied to improve model generalisation and reduce overfitting. These augmentation procedures collectively introduced greater variation into the training set, enabling the models to learn robust, high-level representations and improve classification

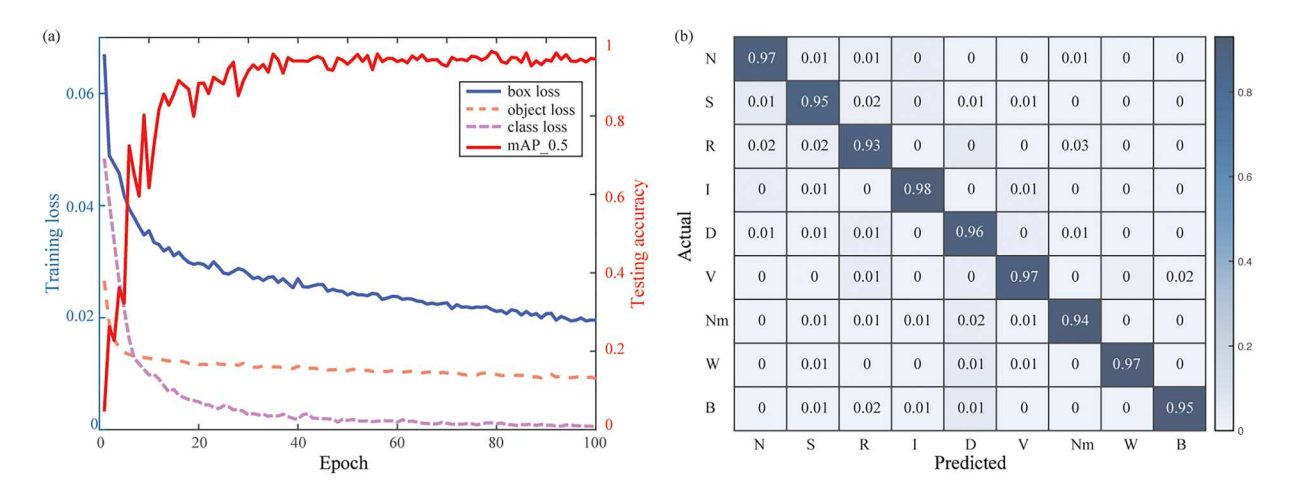


Figure 10. YOLOv5 model development and evaluation: (a) Curves showing the training and testing performance over 100 epochs, and (b) testing performance evaluation matrix highlighting accuracy across different printed line morphologies.

detection performance on unseen data across various defect classes.

Generally, the test accuracies achieved by YOLOv5, EfficientNet, and MobileNetV3 were 96.3%, 91.5%, and 93.2%, respectively. Although direct comparisons between models may be challenging due to their inherent differences, the 96.3% accuracy achieved in FDM anomaly detection is significant, demonstrating the potential and effectiveness of YOLO-based methods in this context. In particular, EfficientNet delivers strong classification performance through the use of mobile inverted bottleneck convolution with channel-wise attention through squeeze-and-excite operations [71], while MobileNetV3 demonstrated superior modelling performance owing to its hardware-optimised inverted residual blocks incorporating spatial and channel attention mechanisms [72], which strategically allocate computational resources to critical features. Conversely, the improved detection accuracy of YOLOv5 results from its complementary architectural design: the CSPNets optimises gradient propagation while reducing computational redundancy, and the PANet enables robust multi-scale defect characterisation through bidirectional feature pyramid fusion [66]. This hierarchical processing allows YOLOv5 to resolve microscopic texture anomalies and macroscopic structural defects simultaneously.

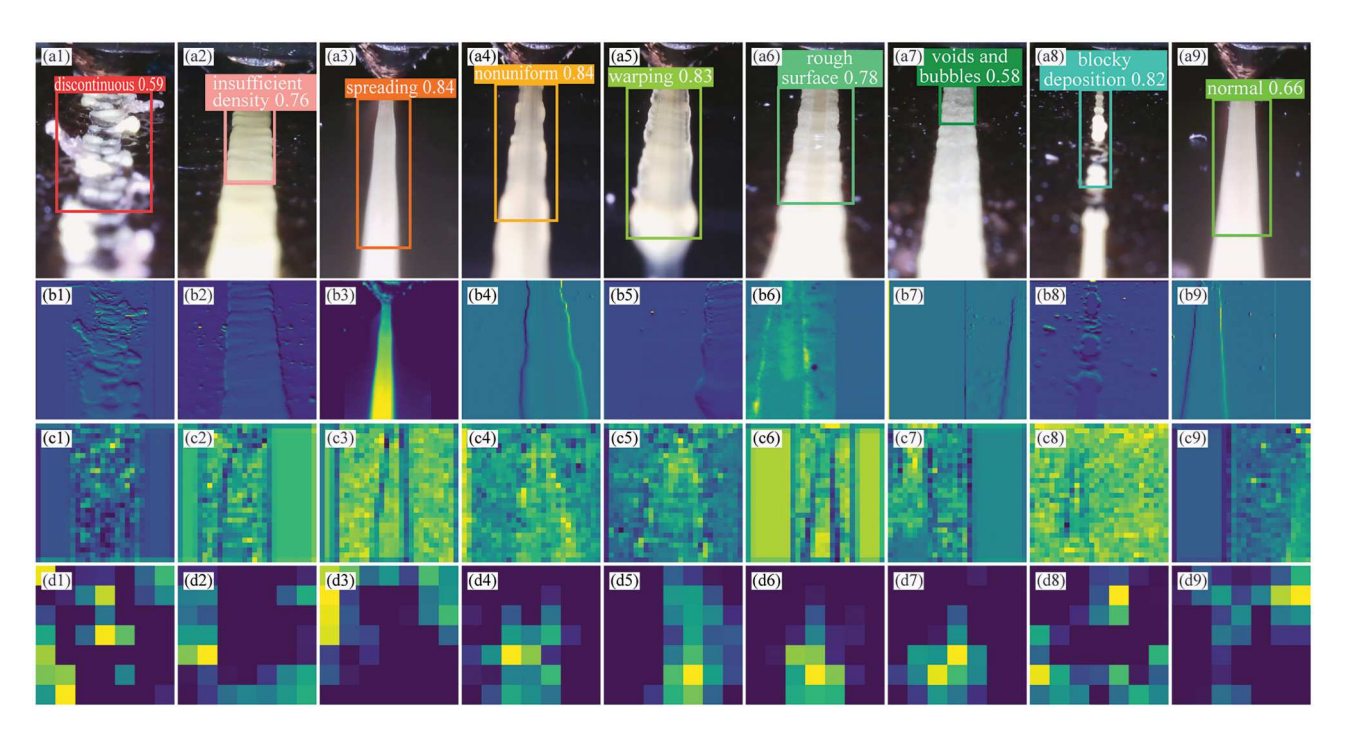


Figure 11. Progressive abstraction in CNN feature learning, (a1-a6) Original input images of printed lines, extracted features after (b1b6) the initial, (c1-c6) the third, and (d1-d6) the final convolutional layer.

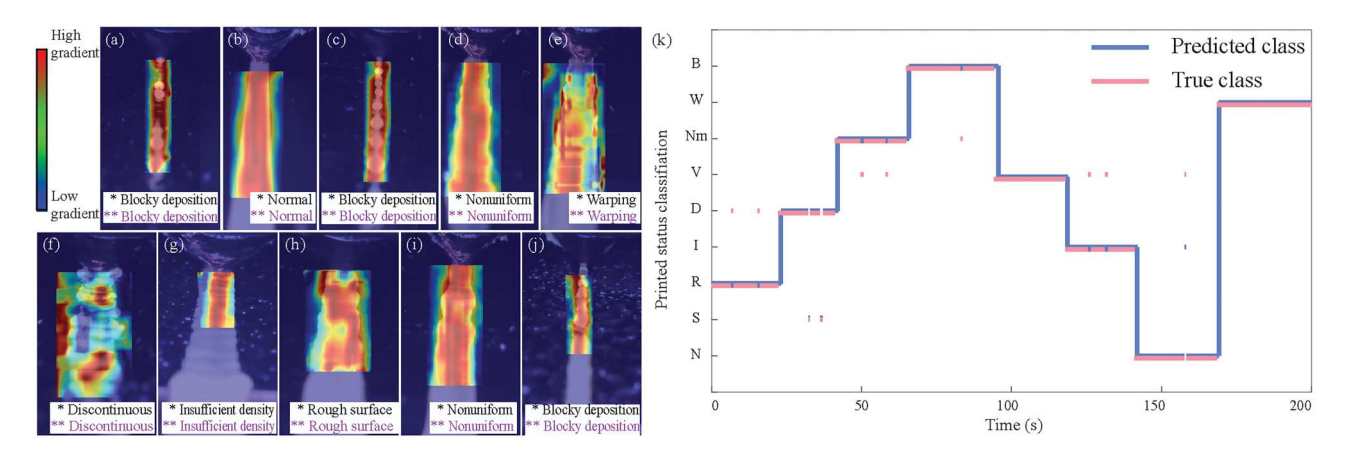


Figure 12. (a–j) Grad-CAM-enhanced YOLO model classification results for FDM, annotated with asterisks (\*true class, \*\*predicted class); (k) Temporal evaluation of the printing status, showing the predicted class distribution (blue) versus the ground-truth profile (red) across sequential printed lines.

Figure 10(a) illustrates the progression of the training and testing performance over epochs of the YOLOv5 model, whereas Figure 10(b) highlights variations in the test accuracy across different printed line morphologies. Lines with insufficient densities exhibit superior accuracy, likely due to their identifiable structural characteristics. Conversely, a rough surface texture in printed lines complicate recognition, as their ambiguous features reduce the discriminability of the model.

#### 3.3.2. Feature analysis of the YOLOv5 model

The YOLOv5 architecture employs a hierarchical feature learning approach, progressively transforming raw pixel inputs (Figure 11(a)) into increasingly abstract representations through successive nonlinear layers. As illustrated in Figure 11, the model begins with initial layers that preserve structural continuity (Figure 11(b)), followed by intermediate layers that focus on detecting orientation-specific edge primitives (Figure 11(c)), and reaching deep layers that leverage multi-scale fusion to resolve complex topologies (Figure 11(d)). This multi-stage processing enables YOLOv5 to effectively handle defect patterns by maintaining sensitivity to subtle variations while capturing robust representations of canonical patterns. The hierarchical structure not only ensures the preservation of fine details in early layers but also facilitates the detection of intricate structures and complex relationships in deeper layers, making the model highly adept at understanding and analysing intricate defect patterns.

# 3.3.3. Abnormality identification and status evaluation for real-time optimisation

The YOLO classifier was employed to categorise images of produced line patterns generated during the FDM process. To introduce variability in the produced line patterns, main adjustable process variables were selected randomly during printing, with the resulting samples recorded using a process camera. To further ensure the prediction accuracy, Gradient-weighted Class Activation Mapping (Grad-CAM) [73], along with a colour bar that associates gradient values with specific colours in the heat map, was integrated with YOLO to generate localisation maps that highlight critical regions within the image. These maps provide an interpretable form of post-hoc attention, offering valuable insights into the model's decision-making process. Figure 12(a-j) presents the classification results of the YOLO model across various printed line characteristics. Even with background changes, the produced lines were consistently classified with high accuracy, highlighting the robustness of the developed classifier. The general performance of the FDM process was derived from the sequence of classification results. Figure 12(k) depicts the FDM printing status, which includes categories such as 'Rough surface texture,' 'Discontinuities,' 'Non-uniform distribution,' and 'Blocky deposition patterns,' among others. Although occasional misclassifications occurred, the predicted status profile (blue lines) closely tracked the true profile (red lines), offering meaningful insights into the evolving dynamics of the FDM process.

Furthermore, the inherent susceptibilities to process instability – including thermal-gradient-induced warping, material shrinkage during cooling, and nozzle extrusion inconsistencies – can compromise the sustainability of the optimised process parameters. This necessitates additional calibration before subsequent printing. In such cases, the identified working status can typically be categorised into one of two different types: normal status (characterised by uniform line deposition) and abnormal status (evidenced by irregular line

Table 4. Basic guidance for online modifications in the FDM process.

	Controllabl	ers	
Detected printing status	Nozzle temperature	Flow rate	Print speed
Discontinuous	7	7	
Insufficient Density	`\		\
Excessive spreading	`	\	7
Rough surface texture	`	\	7
High warping	`	\	7
Nonuniform distribution	\ <u></u>	\	/
Blocky deposition pattern	$\searrow$	/	>
Excessive voids and bubbles	$\searrow$	>	>
Normal	$\rightarrow$	$\rightarrow$	$\rightarrow$

morphology). If an anomaly is detected in the status, real-time modifications to adjustable process variables (e.g. nozzle temperature, flow rate, and print speed) can be implemented using the developed process model. Table 4 shows the basic guidelines for online modifications in the FDM process, prioritising controllable variables in descending order of criticality. For example, if a 'Blocky deposition pattern' is determined, the nozzle temperature should initially be decreased to reduce material viscosity. Next, the flow rate should be increased to compensate for potential under-extrusion, while the print speed is simultaneously decreased to ensure an adequate material deposition volume on the substrate.

On the other hand, while the YOLO model achieves high overall accuracy, it may exhibit conservative misclassifications when faced with ambiguous or edge-case defect patterns. These challenges typically manifest as confusions with neighbouring classes, indicating a slight drop in performance rather than a system failure. To address such scenarios, the system incorporates several key features: attention maps (Figure 12) visualise the model's focus, showing whether uncertain regions are appropriately weighted during classification; temporal consistency checks (Figure 12(k)) evaluate defect predictions across frames to suppress transient misclassifications; and confidence thresholding mechanisms activate additional review processes for low-confidence detections. Together, these strategies maintain system stability during uncertain conditions, with planned enhancements including training set augmentation with edge-case samples and the implementation of uncertainty quantification metrics to further improve ambiguity handling.

#### 4. Conclusion

This work presents a comprehensive data-driven framework that integrates advanced machine learning, deep learning, and real-time computer vision to optimise FDM 3D printing process parameters and enable insitu anomaly detection. The framework employs a stepwise machine learning approach to model and analyse printed line morphologies, ensuring robust pre-print parameter optimisation. For real-time monitoring, a YOLOv5-based object detection model is deployed to assess the stability of the melt flow and to detect morphological anomalies during fabrication. Validation experiments demonstrate the effectiveness of this framework, as it achieves 93.1% accuracy in parameter optimisation and 96.3% precision in defect classification, significantly outperforming conventional empirical (i.e. trial-and-error) and analytical (i.e. simulation-based) methods. A notable contribution of this work lies in its seamless combination of GMM-based morphological classification, SVM-based operational boundary definition, SHAP interpretability, and YOLO-based real-time detection capabilities. This multi-layered integration enables both proactive process planning and reactive correction within a unified, closed-loop control system.

Future research will focus on further enhancing the robustness and scalability of the proposed system across diverse AM environments. Key areas for exploration include: (1) examining varying bed temperatures to optimise process performance, while validating the system across different hardware platforms to ensure real-time applicability; (2) integrating additional quality indicators into the RSM framework, coupled with machine learning models for defect-feature mapping, to improve defect detection and enable more adaptive control strategies; (3) extending the optimisation model to incorporate adaptive extrusion control and advanced slicing algorithms, addressing challenges in material deposition, layer adhesion, and complex geometries; (4) exploring the integration of parameters such as layer thickness and inter-layer bonding to further optimise process parameters and enhance material performance; (5) validating the proposed framework across heterogeneous AM platforms and materials, while leveraging transfer learning techniques to facilitate rapid deployment across diverse platforms without the need for exhaustive retraining; and (6) integrating physics-based models with machine learning approaches to improve model transparency and robustness.



Overall, the proposed methodology advanced FDM manufacturing by integrating data-driven optimisation, in-process anomaly detection, and real-time adaptability. Leveraging advanced machine vision and pattern recognition techniques, it significantly reduces defects, enhances reliability, and offers robust scalability across various AM platforms, including inkjet and direct metal deposition. This approach establishes a strong foundation for process optimisation across multiple domains.

#### **Acknowledgements**

Conceptualisation, H.Z.; methodology, H.Z., Y.Y. and J.P.C.; software, D.S., Y.Y. and H.Z.; validation, Y.K. D.S.; formal analysis, X.L.; investigation, X.L., Y.K. and D.S.; resources, X.L.; data curation, D.S., N.L. and Y.K; writing – original draft preparation, H.Z. and N.L.; writing – review and editing, J.P.C. and S.K.M.; visualisation, H.Z. and Y.K.; supervision, J.P.C. and S.K.M.; project administration, J.P.C.; funding acquisition, J.P.C. and H.Z. All authors have read and agreed to the published version of the manuscript.

#### **Author contributions**

CRediT: **Haining Zhang:** Conceptualization, Funding acquisition, Methodology, Software, Visualization, Writing – original draft; **Yangwen Yu:** Funding acquisition, Methodology, Software; **Xingchen Liu:** Formal analysis, Investigation, Resources; **Nannan Liang:** Data curation, Writing – original draft; **Yongrae Kim:** Investigation, Validation, Visualization; **Dongwoon Shin:** Data curation, Investigation, Software, Validation; **Seung Ki Moon:** Supervision, Writing – review & editing; **Joon Phil Choi:** Funding acquisition, Project administration, Supervision, Writing – review & editing.

#### **Disclosure statement**

No potential conflict of interest was reported by the author(s).

#### **Funding**

This research is supported by the Suzhou University Doctoral Scientific Research Foundation Project (No. 2021BSK023); the Overseas Study Visit Program for Young Backbone Teachers funded by the Anhui Provincial Department of Education (JWFX2023040). This research was also supported by the Basic Research Program funded by the Korea Institute of Machinery and Materials (KIMM) (No. NK255C), and the Technology Innovation Program funded by the Ministry of Trade, Industry, and Energy (MOTIE, Korea) (No. RS-2024-00441774).

#### **Data availability statement**

The raw data supporting the findings of this study are available on the web https://github.com/desmondooo/Optimizaitonfor LM-DIW-viaFDM.

#### References

- [1] Xiong Y, Tang Y, Zhou Q, et al. Intelligent additive manufacturing and design: state of the art and future perspectives. Addit Manuf. 2022;59:103139. doi:10.1016/j.addma. 2022.103139
- [2] Miao G, Du W, Pei Z, et al. A literature review on powder spreading in additive manufacturing. Addit Manuf. 2022;58:103029. doi:10.1016/j.addma.2022.103029
- [3] Sun X, Mazur M, Cheng C-T. A review of void reduction strategies in material extrusion-based additive manufacturing. Addit Manuf. 2023;67:103463. doi:10.1016/j. addma.2023.103463
- [4] Kotadia HR, Gibbons G, Das A, et al. A review of laser powder bed fusion additive manufacturing of aluminium alloys: microstructure and properties. Addit Manuf. 2021;46:102155. doi:10.1016/j.addma.2021.102155
- [5] Awasthi P, Banerjee SS. Fused deposition modeling of thermoplastic elastomeric materials: challenges and opportunities. Addit Manuf. 2021;46:102177. doi:10. 1016/j.addma.2021.102177
- [6] Rett JP, Traore YL, Ho EA. Sustainable materials for fused deposition modeling 3D printing applications. Adv Eng Mater. 2021;23(7):2001472. doi:10.1002/adem.202001472
- [7] Zhang H, Hui J, Lv J, et al. A novel method to combine fused deposition modelling and inkjet printing in manufacturing multifunctional parts for aerospace application. J Mater Res Technol. 2023;24:4405–4426. doi:10.1016/j. jmrt.2023.04.059
- [8] Mallikarjuna B, Bhargav P, Hiremath S, et al. A review on the melt extrusion-based fused deposition modeling (FDM): background, materials, process parameters and military applications. Int J Interact Des Manuf. 2025;19(2):651–665. doi:10.1007/s12008-023-01354-0
- [9] Grivet-Brancot A, Boffito M, Ciardelli G. Use of polyesters in fused deposition modeling for biomedical applications. Macromol Biosci. 2022;22(10):2200039. doi:10.1002/mabi. 202200039
- [10] Mohd Pu'ad NAS, Abdul Haq RH, Mohd Noh H, et al. Review on the fabrication of fused deposition modelling (FDM) composite filament for biomedical applications. Mater Today Proc. 2020;29:228–232. doi:10.1016/j.matpr. 2020.05.535
- [11] Dhinakaran V, Manoj Kumar KP, Bupathi Ram PM, et al. A review on recent advancements in fused deposition modeling. Mater Today Proc. 2020;27:752–756. doi:10.1016/j. matpr.2019.12.036
- [12] Romero PE, Arribas-Barrios J, Rodriguez-Alabanda O, et al. Manufacture of polyurethane foam parts for automotive industry using FDM 3D printed molds. CIRP J Manuf Sci Technol. 2021;32:396–404. doi:10.1016/j.cirpj.2021.01.019
- [13] Zakeri S, Vippola M, Levänen E. A comprehensive review of the photopolymerization of ceramic resins used in stereolithography. Addit Manuf. 2020;35:101177. doi:10. 1016/j.addma.2020.101177
- [14] Xu X, Robles-Martinez P, Madla CM, et al. Stereolithography (SLA) 3D printing of an antihypertensive polyprintlet: case study of an unexpected photopolymer-drug reaction. Addit Manuf. 2020;33:101071. doi:10. 1016/j.addma.2020.101071
- [15] Han W, Kong L, Xu M. Advances in selective laser sintering of polymers. Int J Extreme Manuf. 2022;4(4):042002. doi:10.1088/2631-7990/ac9096



- [16] Kulinowski P, Malczewski P, Pesta E, et al. Selective laser sintering (SLS) technique for pharmaceutical applications—development of high dose controlled release printlets. Addit Manuf. 2021;38:101761. doi:10.1016/j. addma.2020.101761
- [17] Camposeco-Negrete C. Optimization of printing parameters in fused deposition modeling for improving part quality and process sustainability. Int J Adv Manuf Technol. 2020;108(7–8):2131–2147. doi:10.1007/s00170-020-05555-9
- [18] Jaisingh Sheoran A, Kumar H. Fused deposition modeling process parameters optimization and effect on mechanical properties and part quality: review and reflection on present research. Mater Today Proc. 2020;21:1659–1672. doi:10.1016/j.matpr.2019.11.296
- [19] Abeykoon C, Sri-Amphorn P, Fernando A. Optimization of fused deposition modeling parameters for improved PLA and ABS 3D printed structures. Int J Lightweight Mater Manuf. 2020;3(3):284–297. doi:10.1016/j.ijlmm.2020.03.003
- [20] Ameri B, Taheri-Behrooz F, Aliha MRM. Evaluation of the geometrical discontinuity effect on mixed-mode I/II fracture load of FDM 3D-printed parts. Theor Appl Fract Mech. 2021;113:102953. doi:10.1016/j.tafmec.2021.102953
- [21] Maqsood N, Rimašauskas M. Delamination observation occurred during the flexural bending in additively manufactured PLA-short carbon fiber flament reinforced with continuous carbon fiber composite. Results Eng. 2021;11:100246. doi:10.1016/j.rineng.2021.100246
- [22] Hentschel L, Petersmann S, Kynast F, et al. Influence of the print envelope temperature on the morphology and tensile properties of thermoplastic polyolefins fabricated by material extrusion and material jetting additive manufacturing. Polymers (Basel). 2023;15(18):3785. doi:10. 3390/polym15183785
- [23] Kumar A, Collini L, Ursini C, et al. Energy absorption and stiffness of thin and thick-walled closed-cell 3D-printed structures fabricated from a hyperelastic soft polymer. Materials (Basel). 2022;15(7):2441. doi:10.3390/ma15072441
- [24] Wickramasinghe S, Do T, Tran P. FDM-Based 3D printing of polymer and associated composite: a review on mechanical properties, defects and treatments. Polymers (Basel). 2020;12(7):1529. doi:10.3390/polym12071529
- [25] Zhang H, Chen J, Yang D. Fibre misalignment and breakage in 3D printing of continuous carbon fibre reinforced thermoplastic composites. Addit Manuf. 2021;38:101775. doi:10.1016/j.addma.2020.101775
- [26] Guidetti X, Mingard N, Cruz-Oliver R, et al. Force controlled printing for material extrusion additive manufacturing. Addit Manuf. 2024;89:104297. doi:10.1016/j. addma.2024.104297
- [27] Wankhede V, Jagetiya D, Joshi A, et al. Experimental investigation of FDM process parameters using Taguchi analysis. Mater Today Proc. 2020;27:2117–2120. doi:10. 1016/j.matpr.2019.09.078
- [28] Mohan N, Senthil P, Vinodh S, et al. A review on composite materials and process parameters optimisation for the fused deposition modelling process. Virtual Phys Prototyp. 2017;12(1):47–59. doi:10.1080/17452759.2016.1274490
- [29] Dey A, Yodo N. A systematic survey of FDM process parameter optimization and their influence on part characteristics. J Manuf Mater Process. 2019;3(3):64. doi:10. 3390/jmmp3030064

- [30] Popescu D, Zapciu A, Amza C, et al. FDM process parameters influence over the mechanical properties of polymer specimens: a review. Polym Test. 2018;69:157–166. doi:10.1016/j.polymertesting.2018.05.020
- [31] Sood AK, Ohdar RK, Mahapatra SS. Experimental investigation and empirical modelling of FDM process for compressive strength improvement. J Adv Res. 2012;3(1):81–90. doi:10.1016/j.jare.2011.05.001
- [32] Yang L, Li S, Li Y, et al. Experimental investigations for optimizing the extrusion parameters on FDM PLA printed parts. J Mater Eng Perform. 2019;28(1):169–182. doi:10.1007/s11665-018-3784-x
- [33] Samy AA, Golbang A, Harkin-Jones E, et al. Finite element analysis of residual stress and warpage in a 3D printed semi-crystalline polymer: effect of ambient temperature and nozzle speed. J Manuf Process. 2021;70:389–399. doi:10.1016/i.jmapro.2021.08.054
- [34] Nzebuka GC, Ufodike CO, Rahman AM, et al. Numerical modeling of the effect of nozzle diameter and heat flux on the polymer flow in fused filament fabrication. J Manuf Process. 2022;82:585–600. doi:10.1016/j.jmapro.2022.08.029
- [35] Lei M, Wei Q, Li M, et al. Numerical simulation and experimental study the effects of process parameters on filament morphology and mechanical properties of FDM 3D printed PLA/GNPs nanocomposite. Polymers (Basel). 2022;14(15):3081. doi:10.3390/polym14153081
- [36] Paul S. Finite element analysis in fused deposition modeling research: a literature review. Measurement (Mahwah NJ). 2021;178:109320. doi:10.1016/j.measurement.2021.109320
- [37] Fulkerson O, Inman E, Rane A, et al. Multi-objective Bayesian optimization of fused filament fabrication parameters for enhanced specific fracture energy in PLAcarbon fiber composites. Adv Manuf: Polym Compos Sci. 2024;10(1):2395089. doi:10.1080/20550340.2024.2395089
- [38] Khosravi H, Olajire T, Raihan AS, et al. A data driven sequential learning framework to accelerate and optimize multi-objective manufacturing decisions. J Intell Manuf. 2024;35(8):4087–4112. doi:10.1007/s10845-024-02337-y
- [39] Using physics-informed machine learning to optimize 3D printing processes. In Springer tracts in additive manufacturing; Springer International Publishing: Cham, 2023; pp 206–221. doi:10.1007/978-3-031-33890-8\_18
- [40] Kapusuzoglu B, Mahadevan S. Physics-Informed and hybrid machine learning in additive manufacturing: application to fused filament fabrication. JOM. 2020;72(12):4695–4705. doi:10.1007/s11837-020-04438-4
- [41] Li X-Y, Liu F-L, Zhang M-N, et al. A combination of visionand sensor-based defect classifications in extrusion-based additive manufacturing. J Sens. 2023;2023(1): 1441936. doi:10.1155/2023/1441936
- [42] Narayanan BN, Beigh K, Loughnane G, et al. Support vector machine and convolutional neural network based approaches for defect detection in fused filament fabrication. In: Zelinski ME, Taha TM, Howe J, Awwal AA, Iftekharuddin KM, editors. *Applications of machine learning*. San Diego: SPIE; 2019. p. 36. doi:10. 1117/12.2524915
- [43] Özen A, Abali BE, Völlmecke C, et al. Exploring the role of manufacturing parameters on microstructure and mechanical properties in fused deposition modeling (FDM) using PETG. Appl Compos Mater. 2021;28(6):1799–1828. doi:10.1007/s10443-021-09940-9



- [44] Liu Z, Liu Y, He L, et al. A comprehensive investigation of process parameters and material properties effects on printed line quality of aerosol Jet printing based on coupled three-dimensional numerical models. Int J Precis Eng Manuf-Green Technol. 2024;11(3):727-742. doi:10.1007/s40684-024-00604-0
- [45] Hsiang Loh G, Pei E, Gonzalez-Gutierrez J, et al. An overview of material extrusion troubleshooting. Appl Sci. 2020;10(14):4776. doi:10.3390/app10144776
- [46] Di Angelo L, Di Stefano P, Marzola A. Surface quality prediction in FDM additive manufacturing. Int J Adv Manuf Technol. 2017:93(9-12):3655-3662. doi:10.1007/s00170-017-0763-6
- [47] Xie D, Lv F, Yang Y, et al. A review on distortion and residual stress in additive manufacturing. Chin J Mech Eng: Addit Manuf Front. 2022;1(3):100039. doi:10.1016/j. cjmeam.2022.100039
- [48] Kim H, Lee H, Kim J-S, et al. Image-based failure detection for material extrusion process using a convolutional neural network. Int J Adv Manuf Technol. 2020;111(5-6):1291-1302. doi:10.1007/s00170-020-06201-0
- [49] Lu L, Hou J, Yuan S, et al. Deep learning-assisted real-time defect detection and closed-loop adjustment for additive manufacturing of continuous fiber-reinforced polymer composites. Robot Comput Integr Manuf. 2023;79: 102431. doi:10.1016/j.rcim.2022.102431
- [50] Wang L, Jiang J, Dong Y, et al. Machine learning enabled 3D printing parameter settings for desired mechanical properties. Virtual Phys Prototyp. 2024;19(1):e2425825. doi:10.1080/17452759.2024.2425825
- [51] Lu L, Yuan Y, Xie Y, et al. Autonomous intelligent additive manufacturing of continuous fiber-reinforced composites: data-enhanced knowledgebase and multi-sensor fusion. Virtual Phys Prototyp. 2024;19(1):e2412192. doi:10.1080/17452759.2024.2412192
- [52] Saluja A, Xie J, Fayazbakhsh K. A closed-loop inprocess warping detection system for fused filament fabrication using convolutional neural networks. J Manuf Process. 2020;58:407-415. doi:10.1016/j.jmapro. 2020.08.036
- [53] Zhang H, Cui L, Lee P-H, et al. Data-driven autonomous printing process optimization and real-time abnormality identification in aerosol jet-deposited droplet morphology. Virtual Phys Prototyp. 2024;19(1):e2429530. doi:10.1080/17452759.2024.2429530
- [54] Zhang H, Huang J, Zhang X, et al. Autonomous optimization of process parameters and in-situ anomaly detection in aerosol jet printing by an integrated machine learning approach. Addit Manuf. 2024;86:104208. doi:10. 1016/j.addma.2024.104208
- [55] Liu Z, Li M, Weng Y, et al. Mixture design approach to optimize the rheological properties of the material used in 3D cementitious material printing. Constr Build Mater. 2019;198:245–255. doi:10.1016/j.conbuildmat. 2018.11.252
- [56] Zhang H, Choi JP, Moon SK, et al. A hybrid multi-objective optimization of aerosol jet printing process via response surface methodology. Addit Manuf. 2020;33:101096. doi:10.1016/j.addma.2020.101096
- [57] Salary R, Lombardi JP, Samie Tootooni M, et al. Computational fluid dynamics modeling and online

- monitoring of aerosol jet printing process. J Manuf Sci Eng. 2017;139(2):021015. doi:10.1115/1.4034591
- [58] Nohara Y, Matsumoto K, Soejima H, et al. Explanation of machine learning models using shapley additive explanation and application for real data in hospital. Comput Methods Programs Biomed. 2022;214:106584. doi:10. 1016/j.cmpb.2021.106584
- [59] Baptista ML, Goebel K, Henriques EMP. Relation between prognostics predictor evaluation metrics and local interpretability SHAP values. Artif Intell. 2022;306:103667. doi:10.1016/j.artint.2022.103667
- [60] Yang M-S, Lai C-Y, Lin C-Y, A robust EM clustering algorithm for Gaussian mixture models. Pattern Recognit. 2012;45(11):3950-3961. doi:10.1016/j.patcog.2012.04.031
- [61] Paalanen P, Kamarainen J-K, Ilonen J, et al. Feature representation and discrimination based on Gaussian mixture model probability densities—practices and algorithms. Pattern Recognit. 2006;39(7):1346-1358. doi:10.1016/j.patcog.2006.01.005
- [62] Liu Y, Yin S, Liu Z, et al. A machine learning framework for process optimization in aerosol Jet 3D printing. Flex Print Electron. 2023;8(2):025017. doi:10.1088/2058-8585/acd794
- [63] Chorowski J, Wang J, Zurada JM. Review and performance comparison of SVM- and ELM-based classifiers. 2014;128:507-516. Neurocomputing. doi:10.1016/j. neucom.2013.08.009
- [64] Alzubaidi L, Zhang J, Humaidi AJ, et al. Review of deep learning: concepts, CNN architectures, challenges, applications, future directions. J Big Data. 2021;8(1):53. doi:10.1186/s40537-021-00444-8
- [65] Terven J, Córdova-Esparza D-M, Romero-González J-A. A comprehensive review of YOLO architectures in computer vision: from YOLOv1 to YOLOv8 and YOLO-NAS. Mach Learn Knowl Extr. 2023;5(4):1680-1716. doi:10. 3390/make5040083
- [66] Mushtag F, Ramesh K, Deshmukh S, et al. Nuts&bolts: YOLO-v5 and image processing based component identification system. Eng Appl Artif Intell. 2023;118: 105665. doi:10.1016/j.engappai.2022.105665
- [67] Guo Z, Wang C, Yang G, et al. MSFT-YOLO: improved YOLOv5 based on transformer for detecting defects of steel surface. Sensors. 2022;22(9):3467. doi:10.3390/s22093467
- [68] Zhang Y, Guo Z, Wu J, et al. Real-time vehicle detection based on improved YOLO V5. Sustainability. 2022; 14(19):12274. doi:10.3390/su141912274
- [69] Zhang H, Moon SK, Ngo TH, et al. Rapid process modeling of the aerosol Jet printing based on Gaussian process regression with Latin hypercube sampling. Int J Prec Eng Manuf. 2020;21(1):127-136. doi:10.1007/s12541-019-00237-3
- [70] Shields MD, Zhang J. The generalization of Latin hypercube sampling. Reliab Eng Syst Saf. 2016;148:96-108. doi:10.1016/j.ress.2015.12.002
- [71] Tan M, Le QV. EfficientNet: rethinking model scaling for convolutional neural networks.
- [72] Howard A, Sandler M, Chen B, et al. Searching for MobileNetV3. In: O'Conner L, editor. 2019 IEEE/CVF international conference on computer vision (ICCV). Seoul: IEEE; 2019. p. 1314-1324. doi:10.1109/ICCV.2019.00140
- [73] Selvaraju RR, Cogswell M, Das A, et al. Grad-CAM: visual explanations from deep networks via gradient-based localization.

## **Appendix**

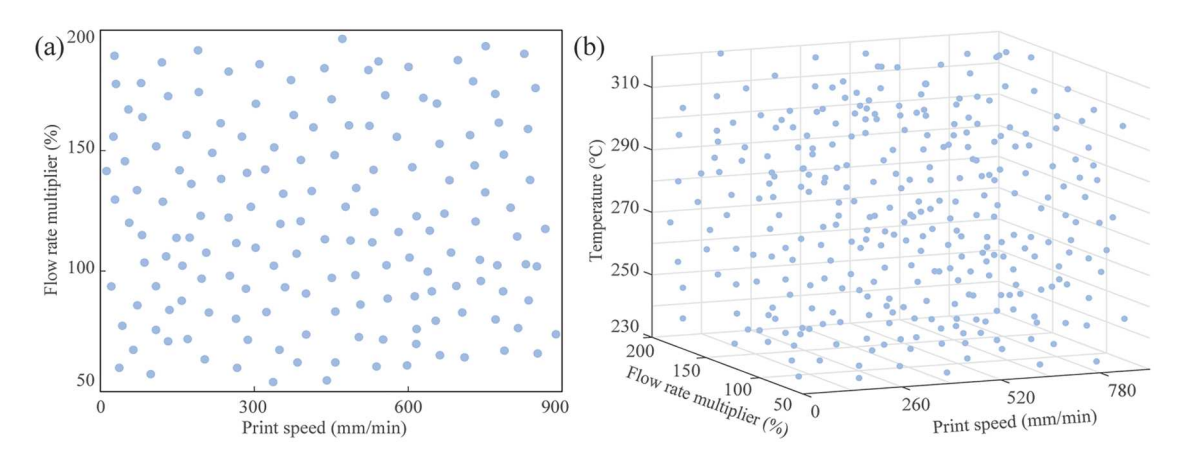


Figure A1. (a) 2D and (b) 3D experimental design based on LHS.

Table A1.	1. The designed experimental points based on CCD.				
NO.	Nozzle temperature	Flow rate multiplier	Pressure advance	Layer thickness	Print speed
1	230	200	2	0.3	60
2	230	200	0	0.1	900
3	230	200	0	0.3	480
4	230	200	0	0.3	900
5	230	50	0	0.3	480
6	230	125	2	0.3	60
7	230	200	0	0.2	60
8	230	50	1	0.1	60
9	230	50	1	0.3	60
10	230	50	0	0.3	900
11	230	200	1	0.3	60
12	230	125	2	0.3	900
13	230	200	2	0.3	900
14	230	200	0	0.2	900
15	230	50	2	0.1	900
16	230	200	2	0.1	480
17	230	200	0	0.1	480
18	230	50	2	0.1	480
19	230	50	2	0.3	60
20	230	50	2	0.3	480
21	230	50	0	0.1	900
22	230	50	0	0.1	60
23	230	125	0	0.1	60
24	230	200	0	0.1	60
25	230	125	1	0.2	480
26	230	125	2	0.1	900
27	230	50	0	0.1	480
28	230	125	0	0.1	900
29	230	50	2	0.1	60
30	230	50	0	0.2	900
31	230	50	0	0.2	60
32	230	200	2	0.2	60
33	230	50	1	0.3	900
34	230	50	2	0.2	60
35	230	125	0	0.3	60
36	230	50	2	0.2	900
37	230	200	1	0.3	900
38	230	200	2	0.2	900
39	230	200	0	0.3	60
40	230	50	2	0.3	900
41	230	125	2	0.1	60
	<del></del>	·- <del>-</del>	_		

(Continued)

Table A1. Continued.

NO.	Nozzle temperature	Flow rate multiplier	Pressure advance	Layer thickness	Print speed
42	230	125	0	0.3	900
43	230	50	0	0.3	60
44 45	230 230	50 200	1 1	0.1 0.1	900 60
46	230	200	2	0.1	60
47	230	200	1	0.1	900
48	230	200	2	0.3	480
49	230	200	2	0.1	900
50	270	125	1	0.1	480
51	270	50	2	0.3	60
52	270	50	0	0.3	900
53	270	200	2	0.3	900
54	270	200	0	0.3	900
55	270	125	1	0.2	60
56 57	270 270	125 200	2 1	0.2 0.2	480 480
58	270	50	1	0.2	480
59	270	125	1	0.2	900
60	270	50	0	0.1	900
61	270	200	2	0.3	60
62	270	50	2	0.3	900
63	270	50	0	0.3	60
64	270	125	0	0.2	480
65	270	50	0	0.1	60
66	270	200	0	0.1	900
67	270	200	2 1	0.1	60
68 69	270 270	125 200	2	0.2 0.1	480 900
70	270	200	0	0.3	60
71	270	200	0	0.1	60
72	270	50	2	0.1	60
73	270	125	1	0.3	480
74	270	50	2	0.1	900
75	310	125	2	0.1	900
76	310	200	0	0.1	480
77	310	200	2	0.2	900
78	310	50	0	0.1	60
79	310	200	2	0.3	60
80	310 310	125 50	1	0.2 0.3	480 900
81 82	310	200	2 2	0.5	480
83	310	50	2	0.2	900
84	310	50	0	0.3	480
85	310	50	2	0.1	480
86	310	200	1	0.3	60
87	310	125	2	0.3	900
88	310	200	2	0.2	60
89	310	200	2	0.3	900
90	310	200	1	0.1	900
91	310	200	0	0.3	480
92	310	200	0	0.2	900
93 94	310 310	200 50	0 1	0.1 0.1	900 900
9 <del>4</del> 95	310	50 50	0	0.1	900
96	310	50	2	0.2	60
97	310	50	0	0.1	900
98	310	50	0	0.3	900
99	310	50	0	0.2	60
100	310	50	0	0.3	60
101	310	125	0	0.1	60
102	310	200	2	0.1	60
103	310	200	0	0.3	60
104	310	50	2	0.2	60
105	310	125	0	0.3	900
106	310	125	2	0.1	60
107	310	50 125	1	0.3	60 60
108 109	310 310	125 200	2 1	0.3	60 900
110	310	200 125	0	0.3 0.1	900 900
111	310	50	2	0.1	900
112	310	50	0	0.1	480
	310	50	· ·	0.1	-100

(Continued)

Table A1. Continued.

NO.	Nozzle temperature	Flow rate multiplier	Pressure advance	Layer thickness	Print speed
113	310	200	2	0.1	900
114	310	200	2	0.3	480
115	310	50	1	0.3	900
116	310	200	1	0.1	60
117	310	50	2	0.1	60
118	310	200	0	0.3	900
119	310	50	1	0.1	60
120	310	200	0	0.2	60
121	310	50	2	0.3	480
122	310	125	0	0.3	60
123	310	200	0	0.1	60

Table A2. The CCD-derived target responses of FDM.

NO.	Printed line width	Printed line edge roughness
1	0.916745	0.1785
2	0.924542	0.279
3	0.571676	0.234
4	0.55009	0.2445
5	0.249528	0.174
6	0.485121	0.14685
7	0.769289	0.2145
8	0.474753	0.14835
9	0.220355	0.168
10	0.23288	0.1845
11	0.577559	0.159
12	0.42313	0.2355
13	0.54892	0.2895
14	0.583024	0.2385
15	0.419111	0.2415
16	0.718254	0.2355
17	0.767227	0.1935
18	0.430501	0.1725
19	0.189625	0.1485
20	0.175821	0.1455
21	0.389129	0.234
22	0.463423	0.1425
23	0.612298	0.159
24	0.706434	0.174
25	0.434146	0.174
26	0.379546	0.1933
27	0.486122	0.2743
28	0.480122	0.2475
29	0.310322	0.2473
30	0.392354	0.144
31		0.1185
32	0.415053	
33	0.72052 0.257517	0.198
		0.207
34	0.402268	0.1485
35	0.48683	0.1845
36	0.363514	0.2085
37	0.610578	0.252
38	0.662934	0.2775
39	0.616564	0.2085
40	0.267647	0.204
41	0.547268	0.1845
42	0.452288	0.2745
43	0.263641	0.144
44	0.501546	0.234
45	0.573436	0.2025
46	0.716579	0.198
47	0.463459	0.249
48	0.546267	0.2205
49	0.715071	0.2565
50	1.528952	0.243
51	0.502167	0.1875
52	0.597895	0.2445
53	1.316118	0.2895
54	1.300706	0.2565
55	1.157656	0.2355

Table A2. Continued.

NO.	Printed line width	Printed line edge roughness
56	1.315482	0.2385
57	1.364491	0.243
58	0.727428	0.174
59	1.095085	0.2865
60	1.016429	0.2475
61	1.321678	0.2355
62	0.562865	0.2475
63	0.570853	0.189
64	1.137866	0.219
65	1.026661	0.1875
66	1.58994	0.2745
67	1.593911	0.231
68	1.091217	0.219
69	1.457779	0.2955
70	1.197111	0.2385
71	1.521596	0.2085
72	0.928766	0.1935
73 74	0.870144	0.2415
74 75	0.873057 1.13601	0.2145 0.234
76 76	1.182443	0.219
77	1.484213	0.2685
78	0.853413	0.2115
79	1.31193	0.2535
80	1.302769	0.2355
81	0.736194	0.234
82	1.234613	0.219
83	0.912173	0.2115
84	0.6906	0.1815
85	1.018778	0.204
86	1.328445	0.2475
87	1.107649	0.237
88	1.579575	0.2535
89	1.358664	0.2415
90	1.736417	0.2385
91	1.341646	0.237
92	1.391095	0.2655
93	1.554903	0.261
94	1.12894	0.2085
95	0.703566	0.2115
96	0.687577	0.2175
97	1.059954	0.234
98	0.496604	0.2355
99	0.569003	0.213
100 101	0.69512 0.969812	0.1875 0.2145
102	1.185984	0.2235
103	1.323643	0.2265
104	0.921788	0.2145
105	1.091977	0.228
106	1.412359	0.2505
107	0.816379	0.2235
108	0.845687	0.2475
109	1.238607	0.2535
110	1.181194	0.258
111	0.725585	0.2115
112	0.69421	0.2025
113	1.416503	0.2685
114	1.070439	0.228
115	0.44891	0.228
116	1.578102	0.2415
117	1.070553	0.213
118	1.209513	0.237
119	0.877836	0.2025
120	1.267229	0.2445
121	0.502593	0.2025
122	0.792841	0.2235
123	1.392783	0.2415